Fundamentals of Electrochemical CO_2 Reduction on Single-Metal-Atom Catalysts

Tu N. Nguyen[1,2,#], Mahdi Salehi[3,#], Quyet Van Le[4], Ali Seifitokaldani[3,*], Cao Thang Dinh[1,*]

[1] Department of Chemical Engineering, Queen's University, Kingston, ON, Canada, K7L 3N6

[2] Helen Scientific Research and Technological Development Co., Ltd, Ho Chi Minh City, Vietnam

[3] Department of Chemical Engineering, McGill University, 3610 University Street, Montreal, QC H3A 0C5, Canada

[4] Institute of Research and Development, Duy Tan University, Da Nang, 550000, Vietnam

[#] These authors contributed equally to this work.

[*] Emails: ali.seifitokaldani@mcgill.ca; caothang.dinh@queensu.ca

Abstract

Electrochemical carbon dioxide (CO_2) reduction powered by renewable electricity offers a path to produce valuable products from CO_2 —this earth-scale human waste— and to store intermittent renewable energy in the form of chemical fuels. Recently, single metal atoms (SMAs) immobilized on a conductive substrate have been shown as effective catalysts for the electrochemical CO_2 reduction, opening the door to a generation of low-cost and high-performance catalysts for fuel and chemical production. The unique physical and chemical properties of a single-atomic structure, the homogeneity of the active sites, combined with tunable coordination environments, are essential for realizing highly active and selective catalysts. In this review, we focus on the structure-performance relationship in SMA catalysts for CO_2 reduction from both theoretical and experimental aspects. We discuss why SMA catalysts exhibit distinct catalytic performance compared to their counterpart nanoparticles. Recent strategies for improving the CO_2 reduction selectivity and activity by tuning the nature and coordination environment of SMA active sites are described. Finally, we highlight potential applications of SMA catalysts in practical CO_2 reduction

conditions, critical challenges, and the path toward efficient electrochemical CO_2 reduction catalysis based on SMAs.

Keywords: Electrochemical CO_2 reduction, Single-metal-atom catalysts, electrocatalysis, structure-performance relationship, CO_2 electroreduction mechanism.

1. Introduction

Reducing greenhouse gas emissions is a major international research priority to avoid the effects of climate change. Achieving this target requires reducing total carbon dioxide (CO_2) emissions by shifting the consumption paradigm from the traditional fossil fuels to low-carbon energy sources such as nuclear, hydro, wind, and solar,[1-2] with the latter two the most abundant renewable energy sources. However, the intrinsic intermittency of solar or wind resources requires long-term and large-scale storage for their further deployment as replacements of fossil fuels.[3-4]

Electrochemical CO_2 reduction (ECR) to fuels and chemicals offer a path to simultaneously address both the CO_2 emission and renewable energy storage challenges.[4-5] ECR enables producing value-added products from CO_2 while enabling the storage of renewable energies in the form of liquid fuels, which can be readily integrated into current infrastructures. The low carbon footprint fuels produced from CO_2 and renewable electricity would play an important role in decarbonizing heavy industries, including chemicals, cement, steel, and transportation, which account for up to 40% of the total CO_2 emission. Converting CO_2 into chemical feedstock enables the sequestration of CO_2 into valuable and long-lifetime products such as polymers.[6]

In ECR, CO_2 is reduced to chemicals at the surface of a catalyst on the cathode of an electrochemical cell. The efficiency of this process strongly depends on the performance of the catalyst. An efficient catalyst for the ECR should drive CO_2 reduction at high current density with high selectivity and stability, and at a low overpotential.[7-9] Currently, metal nanostructures are the most dominant ECR catalysts.[8] Different types of metals have been used to produce a variety of carbon-based products. For example, Ag and Au based catalysts have been demonstrated as efficient catalysts for CO production with high selectivity and activity.[10-15] Selective reduction of CO_2 to formate can be achieved using Pd, Sn, Bi, and Pb-based catalysts.[16-20] Hydrocarbon and oxygenated products beyond C_1 compounds —i.e., compounds with more than one carbon in their chemical structure— have been achieved via ECR using various Cu-based materials.[7, 21-27]

The interaction of the CO_2 molecule and other reaction intermediates with the surface of the catalyst determines the efficiency of the ECR. These interactions influence the reaction pathways, and therefore, the activity and selectivity of the ECR process.[7, 28-29] Several approaches have been developed to fine-tune the interaction between the reactants and the catalyst, including controlling the physical and chemical properties of the catalyst surface, as well as the local reaction

environment. The surface properties of the catalyst can be governed via doping with heteroatoms and controlling particle morphologies or the exposed facets of the catalyst.[30-34] Tuning the reaction microenvironment can be attained through electrolyte engineering or coating the catalyst surface with an overlayer.[21-23] These approaches have been particularly effective in controlling the product distribution in ECR using Cu-based catalysts.

Very recently, single metal atom (SMA) catalysts have emerged as a promising class of catalysts for ECR.[35-38] These catalysts involve SMAs dispersed on a conductive support, predominantly carbon-based materials. Because the size of the catalytic metal species reaches the atomic level in SMA, the unsaturated coordination environment effectively tunes the interaction of CO_2 molecules and reaction intermediates with the active sites. Consequently, SMA catalysts behave very differently from their nanoparticle counterparts in ECR. For example, Ni and Fe nanoparticles exhibit very low CO_2 electroreduction selectivity, producing H_2 as the main product. However, Ni and Fe atoms dispersed on carbon support are highly selective for CO_2 electroreduction to CO.[39-40] Compared to nanoparticulate catalysts, SMA catalysts exhibit higher atom utilization efficiency because all metal atoms are potentially active sites, and can be envisioned as a bridge between heterogeneous and homogeneous catalysis.[41] In addition, the reaction microenvironment in SMA catalysts can be tailored by changing the coordination of active metal sites.[42-43] These features make SMAs promising catalysts for highly efficient ECR.

This review focuses on the structure-performance relationship of SMA catalysts for ECR. Particularly, we discuss how the nature of active sites and its coordination environment govern the activity and selectivity of ECR. We start with a brief introduction about the structure and synthesis of SMA catalysts, followed by describing recent advances in improving both activity and selectivity of the SMA catalysts by tuning the nature of the active site and its coordination environment. We then explain the catalytic properties of SMA catalysts in ECR based on density functional theory (DFT) calculation. Next, we briefly discuss the potential practical application of SMA catalysts by highlighting recent results on industrially relevant ECR systems. Finally, we highlight critical challenges and the path toward efficient ECR catalysis based on SMA catalysts.

2. Single-metal-atom catalysts

2.1. Catalyst structure

SMA catalysts are materials that contain single atoms of metal dispersed on a support without any appreciable interaction between the atoms. For electrocatalytic applications, supports are predominantly carbonaceous substrates, including carbon nanotubes, graphene, and amorphous carbon, although metal oxide substrates have also been reported.[44] Carbon supports exhibit high electrical conductivity for fast electron transport and high surface area which enables high active catalyst loading (**Figure 1a**). In addition, carbon-based supports exhibit very low activity toward hydrogen evolution reaction (HER), which is a critical property of the support for ECR applications. Due to their high surface energy, metal atoms need to chemically bond to the surface of the support to be stable. Active metals for ECR are mainly Ni, Co, Fe, Cu, and Zn, which bind weakly to the carbon atom on the substrate. Thus, stabilization of metal atoms is often achieved via the binding with defect sites or dative bonds to other heteroatoms on the carbon support such as N, S, P, and O (**Figure 1b**).

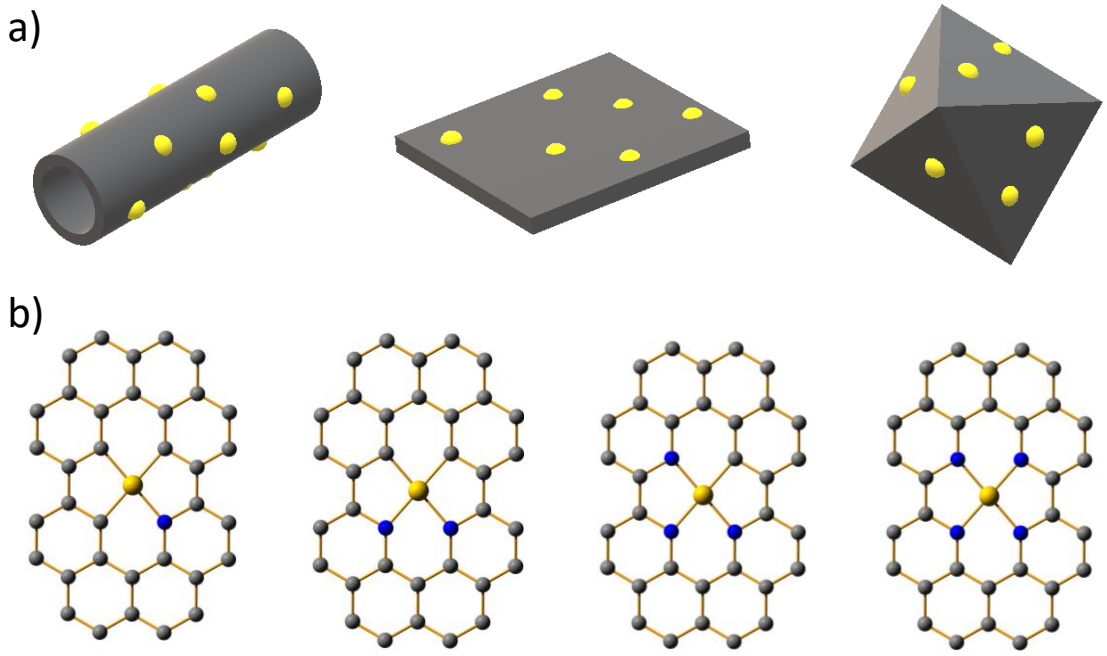

Figure 1. a) Single-metal-atom catalyst (yellow balls) immobilized on substrates with different morphologies; b) different coordination configurations of SMAs on the support. Yellow balls are SMAs, blue balls are coordination elements, and grey balls are carbon atoms.

The coordination of metal atoms with the surface not only prevents their aggregation but also changes the electronic and geometric structures of the metal active sites. For example, the strong or weak electron-donating effect from the heteroatoms on the carbon substrate to the SMA might alter the interaction of the metal atom with CO_2 and reaction intermediates. It can also be envisioned that the catalytic activity might be different for a metal atom that possesses symmetric versus asymmetric geometry or is positioned in-plane versus out-of-plane of the substrate. Tuning the metal-support interaction is, therefore, a powerful tool to improve the catalytic performance of SMA catalysts.

SMAs are usually undercoordinated, which renders them electrochemically active material. Therefore, besides the nature of the coordination atoms, the coordination number, which affects the electronic structure of the active site, also plays a crucial role in tuning the activity of SMA catalysts. Decreasing the coordination number is often observed (but not always) to enhance the interaction between the metal atom and CO_2 and reaction intermediates;[45] however, this can be a trade-off for the stability of SMAs on the support. DFT calculations considering the optimized configuration of N-doped graphene towards stable SMAs suggested that the coordination number ≤ 2 is not likely to provide sufficient binding energy to metal atoms to stabilized SMAs, whereas a coordination number 4 can allow immobilization of late transition SMAs such as Fe, Co, Ni, and Cu.[46] It is worth noting that increasing the coordination number by introducing an additional axial ligand is also a strategy to tune the energy level of *d* orbitals and the energy barrier for CO_2 binding, allowing for improving the catalytic activity of SMAs.

2.2. Synthesis

The synthesis of SMA catalysts for ECR involves the deposition of metal atoms and coordination elements on conductive carbon-based substrates. Many methods, such as electrochemical deposition, physical deposition, and wet-chemistry pyrolysis, have been used to achieve this goal. The synthesis of SMAs can involve multiple steps, including the precursor preparation and the formation of the support, the active sites, and coordination elements. In this review, we categorize the synthesis of SMAs into three main routes based on the sequence of physical and chemical processes involving the formation of metal active sites and the coordination elements. They include (1) Deposition of SMAs on modified carbon support: the SMAs and coordination elements are deposited on support in two separate processes; (2) Co-deposition of SMAs and coordination

elements on carbon support: the SMAs and coordination elements are formed simultaneously in a single process; and (3) One-pot synthesis of SMAs and carbon support: the SMAs, coordination elements, and carbon support are formed simultaneously in a single process.

2.2.1. Deposition of SMAs on modified carbon support

This approach involves the preparation of carbon support containing coordination elements in the first step, followed by the deposition of metal atoms on the support in the second step. The deposition of SMAs on modified carbon support has the advantage of controlling the active metals, coordination elements, and carbon support separately, enabling catalysts with fine-tuned structure and composition. The synthesis of carbon support modified with coordination elements can be achieved via a direct synthesis or a post-treatment approach. For example, N-doped graphene can be grown by chemical vapor deposition using H_2, and methane (CH_4) and ammonia (NH_3) as carbon and N sources, respectively. This method gives rise to graphitic-N as the major configuration, whereas pyridinic-N and pyrrolic-N were found to be minor species.[47] The structure and composition of the modified carbon support depend on both carbon and nitrogen sources and reaction temperature. Luo et al. achieved pure pyridinic-N by using H_2, ethylene, and ammonia gas with an N content of up to 16 wt%,[48] which is much higher than the content of a few wt% often observed in N-doped graphene materials. Wang et al. successfully modulated the configuration of N atoms in N-doped graphene to pyrrolic-N using imidazole ($C_3H_4N_2$) and poly(methyl methacrylate) as N and C sources.[49] The post-treatment method in which N atoms are doped into a preformed carbon support, was also found to be an effective method for producing N-doped carbon with controllable N-configuration. The three most common approaches to introduce N into pristine graphene upon post-treatment are ammonia exposure,[50] nitrogen ion implantation,[51] and nitrogen plasma.[52] Graphene materials functionalized with groups such as cyanide and carboxylic acid can also be prepared via the post-treatment of the fluorographene.[53]

The deposition of metals on a modified carbon substrate can be achieved via various methods, including physical deposition, photochemical reduction, mechanical ball-milling, and thermal treatment. Atomic layer deposition (ALD), which is based on the sequential exposure of the substrate's surface to gaseous precursors, is one of the common physical deposition methods. A typical example of loading SMAs onto N-doped graphene using ALD was reported by Stambula et al.[54] The authors observed Pt-SMAs and clusters up to 150 ALD cycles without the formation

of nanoparticles. Similarly, Cheng et al. observed a large amount of Pt-SMAs up to 100 ALD cycles of deposition. After 100 cycles, a considerable amount of Pt particles appeared due to aggregation.[55] It is worth noting that the applicability of the ALD technique for large-scale synthesis of catalysts is limited, inhibiting its use for commercially relevant applications.

SMAs can also be deposited on modified carbon substrates via the photochemical reduction method, which often involves the use of ultraviolet light to reduce metal ions. Li et al. reported the photochemical solid-phase synthesis of platinum single atoms on N-doped carbon without the formation of clusters or nanoparticles.[56] In this method, N-doped carbon was first dispersed into an aqueous solution containing Pt precursor, allowing the adsorption of Pt precursor onto the N-doped carbon surface. Illuminating the resulting solid with ultraviolet light gave rise to Pt SMAs. This method allowed for achieving relatively high Pt loading (up to 3.8 wt %); however, it is not employed for non-noble metals, mainly due to the limited reducing capability of ultraviolet light.

The ball milling method relies on high-speed moving balls that transfer their kinetic energy to the material, allowing for reconstructing the material's surface and inducing chemical bonding. For example, the ball-milling of a mixture of iron phthalocyanine (FePc) and N-doped graphene yielded Fe-SMAs with a loading content of 4 wt%, which is relatively high since the loading reported for Fe-SMAs is often less than 2 wt%. The utility of FePc was up to 90%, suggesting that the ball-milling process provides sufficient input energy to break the chemical bond of the metal precursor to form isolated Fe atoms on N-doped graphene. This method was further extended to synthesize other SMAs such as Mn, Co, Ni, and Cu.[57]

The chemical deposition is a rather benign method to introduce SMAs on a modified carbon substrate. This method involves the deposition of a metal precursor on a modified carbon support, followed by the reduction of the metal cations via a chemical reduction process or a thermal treatment under a reducing environment. SMAs of a variety of metals, including Co, Ni, Fe, Bi, and Cu, with precise control over the metal loading, have been achieved using the chemical deposition method (**Figure 2a**). [58-61] The simplicity of this impregnation method is encouraging for designing SMA catalysts in a controlled fashion and with different metal active sites.

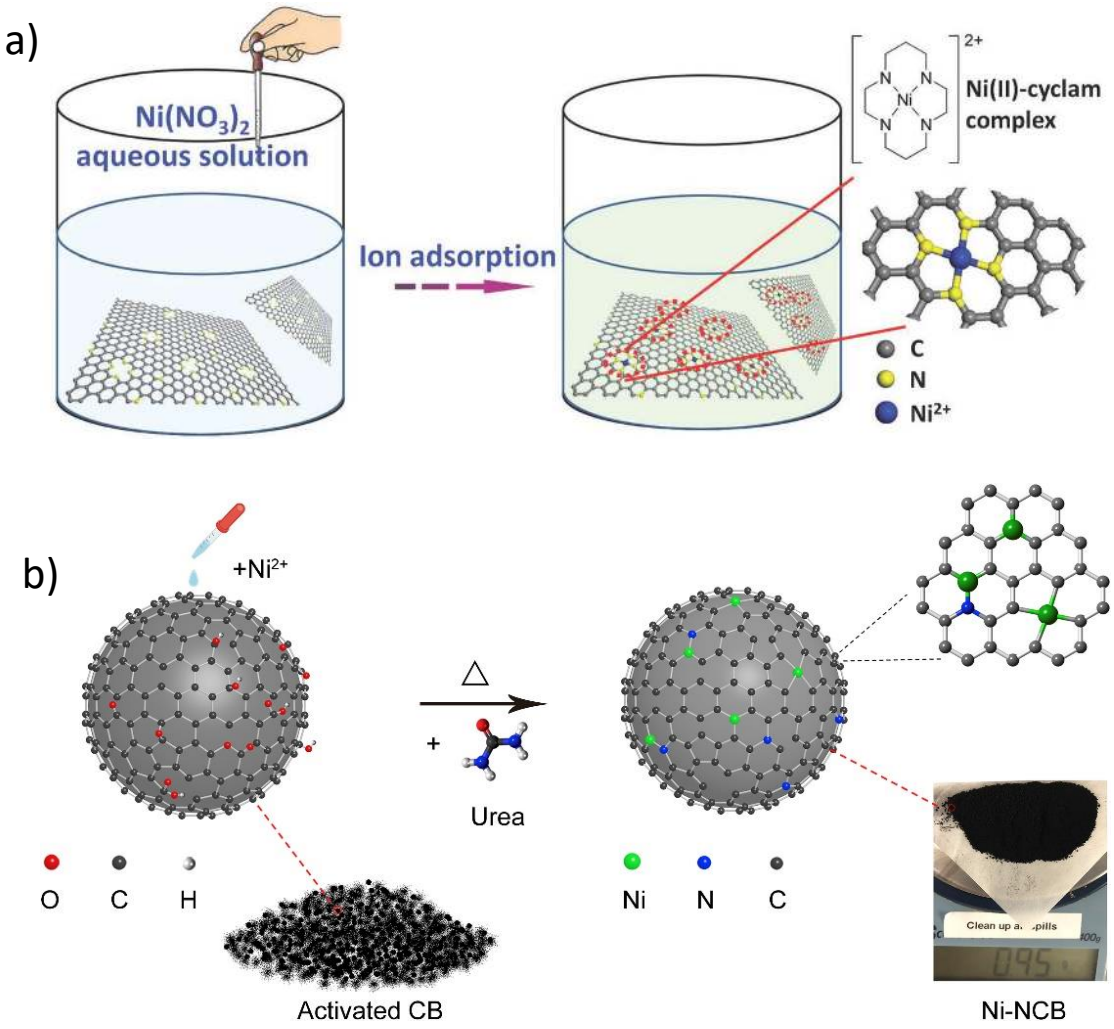

Figure 2. a) Schematic illustration of surface immobilization of transition metal ions on N-doped graphene via ion adsorption. The inset compares the structure of Ni^{2+}@NG and Ni(II)-cyclam complex. Reproduced with permission from reference [59]. Copyright 2018 Wiley; b) Co-deposition of Ni and N on activated carbon black (CB) to Ni SMA catalysts. Reproduced with permission from reference [62]. Copyright 2019 Elsevier.

2.2.2. Co-deposition of SMAs and coordination elements on carbon support

In this approach, metal atoms and coordination elements are formed on carbon support in a single process. One of the precursors is often predeposited on the carbon support, followed by a thermal treatment via pyrolysis or microwave radiation in the presence of another precursor to simultaneously incorporate metal and coordination elements into the matrix. For example, Zheng

and coworkers used commercially available carbon blacks (CBs) with an activated surface to adsorb Ni cations in the first step. Treatment of the Ni/CB with urea as the N source produced Ni SMA catalyst (Ni-NCB) (**Figure 2b**).[62] Zhao et al. reported an approach to synthesize a wide range of atomically dispersed M-N_x on carbon support (M = Mn, Fe, Co, Ni, Cu, Mo, Pt).[63] The preparation involved the chelating of the metal precursor on glucose, which was grounded with melamine as the N source, followed by a pyrolysis process at 800 ^{o}C. Alternatively, gases containing the coordination element precursors, such as ammonia and hydrogen sulfide, can be used for the co-deposition of metal and coordination elements on carbon substrates. This method was introduced by Tour and coworkers for the first time in 2015 for the preparation of Co-SMAs on N-doped graphene.[64] It has also been employed for the preparation of SMAs of Ru, Ni, Fe, and Mn. [65-68]

The thermal annealing method often involves prolonged heating treatment, which can cause aggregation of metal atoms. Microwave radiation is an alternative method that allows for obtaining SMAs in a much shorter period, e.g., a few seconds, reducing side reactions as well as metal aggregation. For example, Fei et al. performed microwave irradiation on a freeze-dried mixture of amine-functionalized graphene and a trace amount of Co precursor to achieve Co-SMAs on N-doped graphene. This method was also adopted to synthesize Cu- and Ni-SMAs.[69] Despite its simplicity and rapid synthesis, this method is barely investigated by other research groups so far. The extension of this method to obtain either other types of SMAs or higher SMAs loading needs to be considered further.

2.2.3. One-pot synthesis of SMAs on carbon support

In the one-pot synthesis, precursors of metal, carbon, and coordination atoms are mixed and undergo thermal treatment to form SMAs on substrates. A common strategy is the employment of metal-organic frameworks (MOFs), which are crystalline porous materials that often exhibit large surface area and tunable chemical structure.[70] The ability to dope different metals and tailor the ligand as the source for both carbon and coordination atoms makes MOFs appealing for the preparation of SMAs. It has been shown that the thermal decomposition of MOFs in a suitable atmosphere leads to the formation of carbon-based materials with MOF-like structures, inheriting most of MOFs properties, including large surface area and porosity.[71-72] Upon high-temperature thermolysis, metal ions or clusters, which are periodically distributed in MOFs, can migrate along

the surface of mesoporous carbon and associate with defects on the carbon network such as vacancies or adatoms (N, S) to form SMAs. To date, N adatoms (N-defects) have been demonstrated to be the most active sites for SMAs to be stabilized on MOF-derived carbon materials (MOF-NCs).

To confine SMAs on MOF-NCs, factors in the design of MOFs, including the proper amount of metal ions, types of metal ions, MOF cages, and N species, need to be thoroughly considered. In addition, pyrolysis conditions such as temperature and atmosphere should be taken into account. The first attempt to obtain SMAs on MOF-NCs was carried out by Zitolo et al. in 2015.[73] The synthesis of Fe-SMAs on MOF-NCs was completed via two steps. First, a composite powder comprises of Zn^{2+} zeolitic imidazolate framework (Bassolite Z12000 (ZIF-8)), Fe^{2+} acetate, and 1,10-phenanthroline was ball-milled in a zirconium oxide crucible to obtain a homogeneous precursor. In the next step, highly pure Fe-SMAs on MOF-NCs were achieved by annealing of the prepared precursor at 1050 °C in an Ar or NH_3 atmosphere. Other efforts to improve the SMA loading on MOF-NCs have been recently reported. For example, Jiao et al. utilized mixed ligands comprised of Fe-tetrakis (4-carboxyphenyl)porphyrin (Fe-TCPP) and H_2-TCPP to render the Fe atom into the PCN-222 MOF (PCN stands for porous coordination network) (**Figure 3a**).[74] The percentage of Fe in PCN-222 can be modulated by varying the Fe-TCPP and H_2-TCPP ratio. The pyrolysis of an optimized Fe-PCN-222 MOF yielded Fe-SMAs in MOF-NCs. Chen et al. came up with another strategy by covering $Fe(acac)_3$ precursors within the cages of ZIF-8 (**Figure 3b**).[75] The cages inhibited the immigration of Fe atoms upon pyrolysis, resulting in Fe-SMAs on MOF-NCs. In another work that was also conducted by this group, they discovered that the ionic exchange takes place at a high temperature during pyrolysis while preparing Ni-SMAs (**Figure 3c**).[76] Typically, Ni ions were impregnated into ZIF-8, followed by a pyrolysis process. At hight temperature (ablove1000 °C), Zn^{2+} tends to be reduced and evaporated, leaving MOF-NCs with high N defects. These defects subsequently attract nearby Ni^{2+} to form Ni-SMAs. However, if an excessive amount of Ni ions were incorporated into ZIF-8, Ni nanoparticles were inevitably generated instead of Ni-SMAs. Because of this limitation, the loading of Ni-SMAs on MOF-NCs was reported to be around 1.53 wt%. More recently, a work by Yin et al. improved the loading of SMAs on MOF-NCs up to 4 wt% using Zn/Co bimetallic MOFs.[77] The authors hypothesized that the Zn^{2+} in MOFs is devoted to the defect formation upon evaporation. Moreover, because Zn and

Co are homogeneously distributed in the MOF structure, Zn acts as a fence to impede the aggregation of Co into nanoparticles, thus promoting a high loading of Co-SMAs.

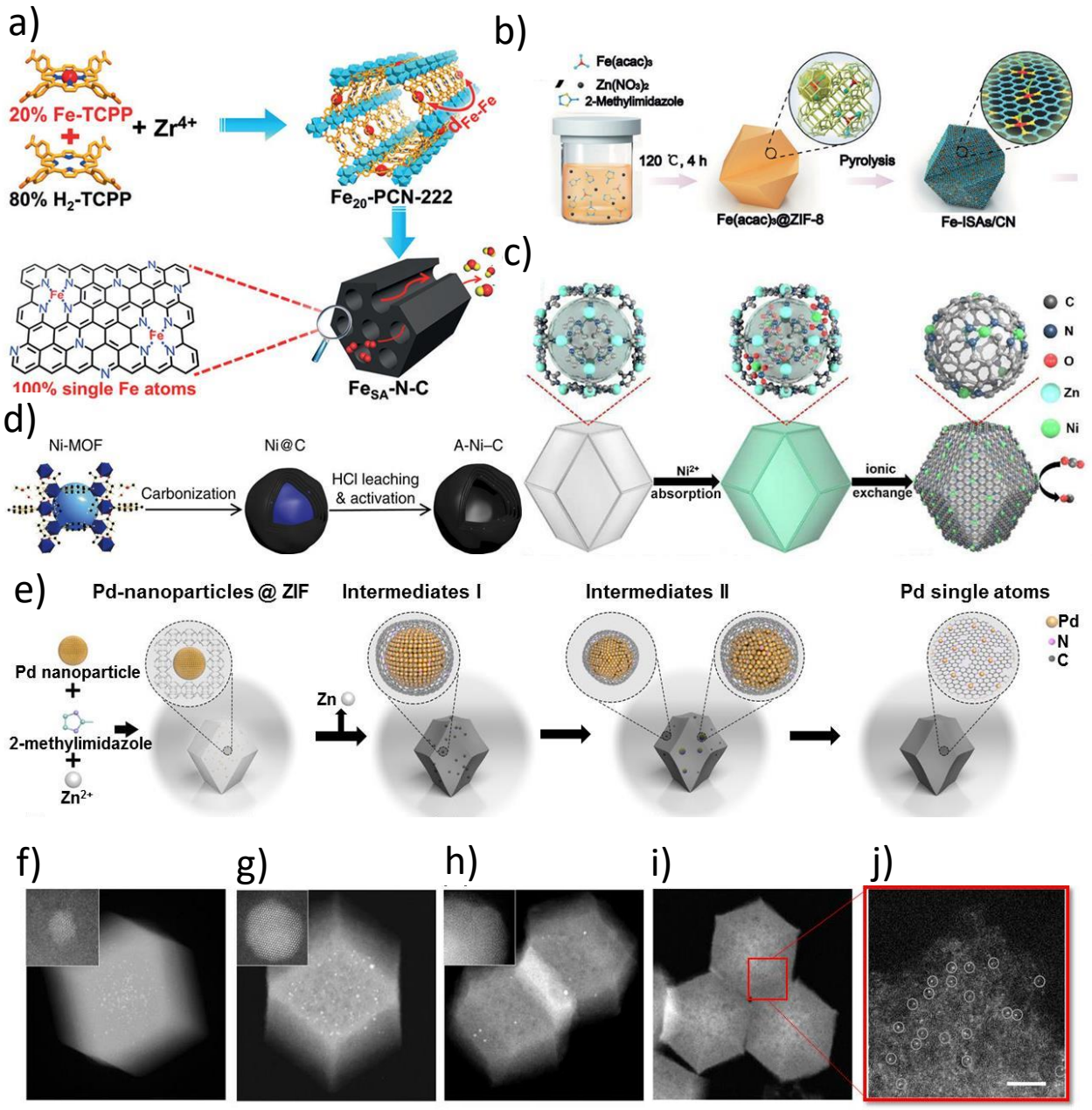

Figure 3. a) Illustration of the fabrication of Fe-SMAs/N-C catalyst via a mixed-ligand strategy. Reproduced with permission from reference [74]. Copyright 2018 Wiley; b) Schematic illustration of the formation of Fe-SMAs/MOF-NCs via cage encapsulated-precursor pyrolysis. Reproduced with permission from reference [75]. Copyright 2017 Wiley; c) Scheme of the formation of Ni-SMAs/MOF-NCs via ionic exchange. Reproduced with permission from reference [76]. Copyright

2017 American Chemical Society; d) Schematic diagram of synthesis and activation process of the Ni-SMAs/MOF-NCs via electrochemical activation. Reproduced with permission from reference [78]. Copyright 2016 Nature; e) Scheme of the transformation of NPs to single atoms and structural characterizations of Pd single atoms; f-j) HAADF-STEM images and high-resolution HAADF-STEM images (insets) of Pd-NPs@ZIF-8 (f), intermediate I (g), intermediate II (h) and Pd single atoms (i-j). The scale in (j) is 2 nm. Reproduced with permission from reference [79]. Copyright 2018 Nature.

Besides tuning the MOF's structure, modulation of pyrolysis conditions also has a critical impact on the formation of SMAs in MOF-NCs.[79] Wei and co-workers found that prolonged thermal treatment of M-ZIF-8 (M: Pd, Pt, Au) resulted in the conversion of metal nanoparticles to SMAs (**Figure 3e**).[79] The atomization of nanoparticles to SMAs can be interpreted into 3 steps. At the initial stage in which the temperature reaches 900 °C, the diameter of the nanoparticles gradually increases, whereas the number of nanoparticles decreases, suggesting the coexistence of sintering and atomization. When the temperature is further increased up to 1000 °C, either the sintering or atomization rate rapidly enhances. At this high temperature, these nanoparticles are supposed to vaporize, ultimately disappear. The mobile M-atoms subsequently diffuse through the surface of MOF-NCs and are captured by N-defects in MOF-NCs. Another strategy to get SMAs in MOF-NCs is to use electrochemical activation, which was reported by Fan et al. (**Figure 3d**).[78] However, this method is scarcely investigated by other groups so far.

Besides the employment of MOF structures, the combination of other precursors of metal, carbon, and the coordination atoms for the preparation of SMAs was also demonstrated. For example, Zhu et al. discovered that the decomposition of the silk cocoon protein resulted in highly doped N with pyridinic-N and pyrrolic-N as main products.[80] Thus, several types of SMAs such as Co, Ni, and Fe were immobilized on to N-doped graphene by annealing metal salts and silk fibroin composite under the Ar atmosphere at 900 °C. In the one-pot synthesis method, metal salts are usually used as metal precursors while glucose and amine compounds can be used as carbon and nitrogen sources, respectively. This method has been used for the synthesis of SMAs of various metals, including Pt, Pd, Ni, Co, and Fe. While the one-pot synthesis is simple, precise control over the structure of the SMAs is difficult to achieve with this method. [81-83]

3. Structure-performance relationship of SMA catalysts in ECR

The performance of SMAs depends on two key factors: the nature of the active metals and the nature of the coordination environment, including coordination elements and coordination number.

3.1. Effect of the nature of active sites

The identity of the SMA active site has a significant impact on the selectivity of the products. A common structure of SMAs is the metal atom coordinated by four pyridinic N atoms from the N-doped carbon substrate. Below, we review several SMA catalysts with this configuration and discuss their performance for ECR.

3.1.1. Ni SMA catalysts

Ni-based SMAs are the most studied among SMA catalysts for ECR, with CO being the main product. One of the early works describing exclusive Ni-pyridinic N_4 sites on N-doped graphene (Ni-N_4-C) for ECR was reported by Li et al. [39] (**Figure 4a**). The single-atom sites were confirmed by extended X-ray absorption fine structure (EXAFS) measurements and visualized by the HAADF-STEM image (**Figure 4b**). With Ni-N_4-C as the electrocatalyst, the authors observed that the HER was significantly suppressed, which is drastically different from Ni nanoparticles that favor the H_2 production. DFT calculations revealed that the introduction of Ni−N_4 sites favors the formation of *COOH on Ni−N_4−C compared to that of N−doped graphene alone (**Figure 4c**). Moreover, the difference between the thermodynamic limiting potentials for CO_2 reduction and H_2 evolution ($U_L(CO_2) - U_L(H_2)$) is more positive for Ni−N_4−C, suggesting the higher selectivity for the reduction of CO_2 to CO than for the competitive H_2 evolution. This prediction was experimentally demonstrated, as high selectivity near unity for CO formation was obtained for Ni−N_4−C, and the current density reached 28.6 mA cm^{-2} at -0.81 V. This performance is equal or even better than that of electrocatalysts based on noble metals such as Ag and Au with similar electrochemical cell settings.[13-14] Similar performance of Ni-pyridinic N_4 SMAs for ECR was also observed in Ni^{2+}@NG and Ni^{2+} on N-doped carbon nanotubes (NiSA-N-CNTs) reported by Bi et al. and Cheng et al., respectively.[59, 84] Notably, the high Ni loading content in the latter, of 20 ± 4 wt% compared to less than 1 wt% in the former, did not show an improvement of catalytic activity, suggesting that not all SMAs are catalytically active as these sites might be buried within the substrates. Comparing to the pristine carbon substrates, which can also catalyze the ECR reaction to CO, the Ni single-atom catalysts exhibit enhanced catalytic activity due to their much lower interfacial charge-transfer resistance as shown in the Nyquist plot (**Figure 4d**), which facilitates

the kinetics of CO_2 reduction.[59] In all cases, the Ni single-atom catalysts are relatively stable, displaying retention of a current density and Faradaic efficiency for tens of hours, and the atomically dispersed Ni atoms did not show noticeable aggregation. When Ni^{2+} ions were replaced by Fe^{3+} or Co^{2+}, the CO selectivity decreased following the order Ni^{2+} > Fe^{3+}> Co^{2+}. This trend was explained based on the different interactions between these active sites and CO, with Co^{2+} exhibiting a strong CO binding, poisoning the active sites, and hence favoring the competing HER.[59]

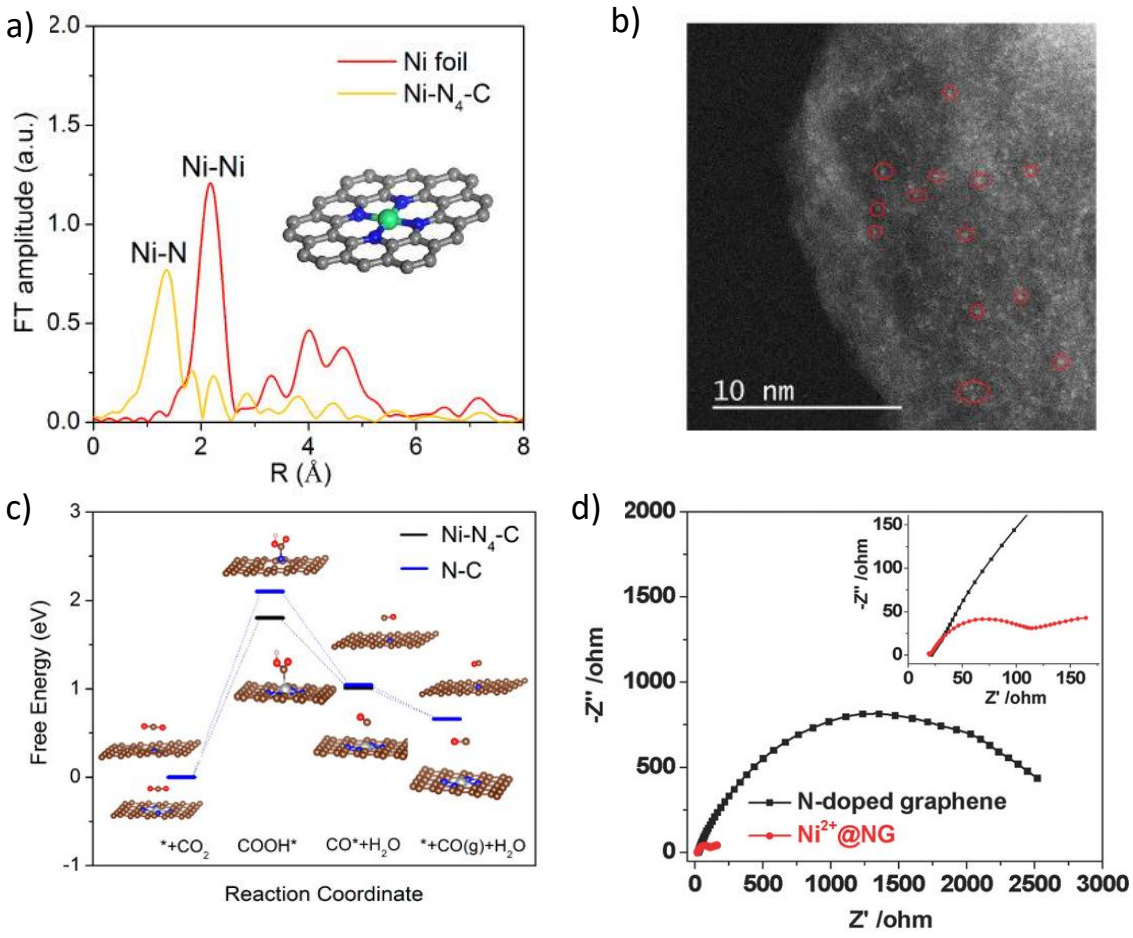

Figure 4. a) Fourier transformation of the Ni K-edge EXAFS oscillations of Ni–N_4–C (the structure is shown in inset); b) HAADF-STEM image of Ni−N_4−C; c) Calculated free energy diagram of CO_2 reduction for Ni−N_4−C and N−C. Reproduced with permission from reference [39]. Copyright 2017 American Chemical Society; d) Nyquist plots of Ni^{2+}@NG in comparison with N-doped graphene. The inset shows a locally amplified view. Reproduced with permission from reference [59]. Copyright 2018 Wiley.

3.1.2. Co SMA catalysts

Co SMAs are often studied for CO_2 reduction to CO, but the Co-N_4 sites with pyridinic N atoms have been observed to have lower activity compared to that of the Ni counterparts.[39, 59, 84] Nevertheless, Co-N_4 sites are still interesting catalytic sites for the formation of other products besides CO, such as methanol (MeOH), due to the strong interaction between the Co single atoms and the reduction intermediates. Wu et al. prepared Co-SMA-based catalysts by depositing cobalt phthalocyanine (CoPc) complexes on CNTs (**Figure 5a, b**) and found that the CoPc/CNT produced MeOH with FE_{MeOH} of 44%, together with CO and H_2.[85] This level of selectivity toward MeOH is rarely observed besides the Cu-based SMAs,[86] and is fundamentally interesting although it is still low for practical applications. The domino mechanism for the formation of MeOH was proposed (**Figure 5c**), in which CO_2 first undergoes a two-electron reduction to CO, and then further reduced through a four-electron–four-proton process. CoPc/CNT was found to be not stable for long-term electrolysis, with the FE_{MeOH} significantly diminished to 0.6% after 5 hours, which was attributed to the hydrogenation on the pyrrole rings of Pc. To tackle this issue, the authors introduced four electron-donating $–NH_2$ groups to the β positions of the Pc ligand (**Figure 5d**), lowering the reduction potential of CoPc. The CoPc–NH_2/CNT catalyst exhibited similar performance to that of CoPc/CNT (**Figure 5e**), while the stability of the catalyst was improved, as the measured FE_{MeOH} remained stable after 12 hours of electrolysis (**Figure 5f**).

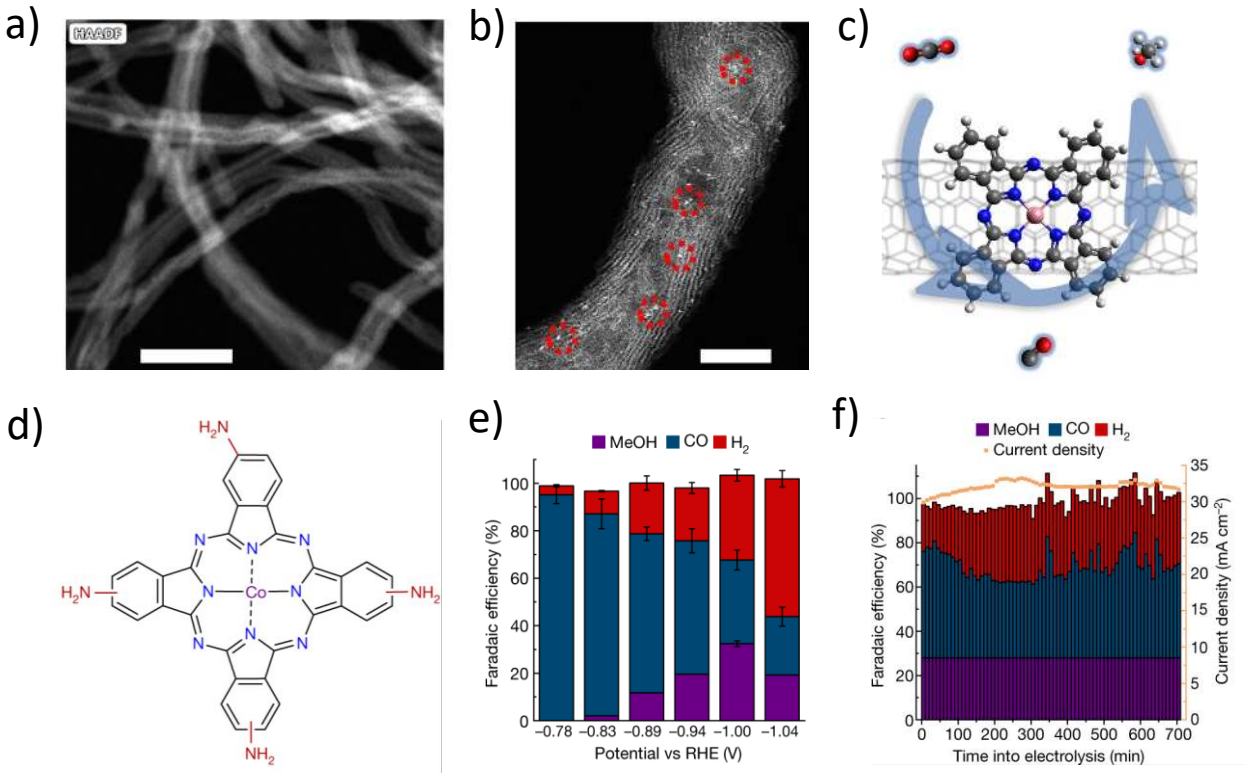

Figure 5. a) STEM-HAADF image of CoPc/CNT; b) Atomic-resolution STEMH-AADF image of CoPc/CNT. The circled bright spots correspond to the Co center of individual CoPc molecules. Scale bars, 50 nm (a) and 5 nm; c) Domino process of CO_2-to-MeOH conversion via CO, catalyzed by CoPc supported on carbon nanotubes (CNT); d) CoPc–NH_2; e) Potential-dependent product selectivity; f) Product selectivity and total current density for a 12-hour electrolysis of CO_2 reduction catalyzed by CoPc–NH_2/CNT at −1.00 V vs. RHE. Reproduced with permission from reference [85]. Copyright 2019 Nature.

3.1.3. Fe SMA catalysts

The Fe-N_4 sites with pyridinic N atoms have also been demonstrated for CO_2 reduction to CO, with a slightly lower catalytic activity compared to that of the Ni-N_4 sites;[39, 59, 84] but more reactive than other transition metals such as Co, Mn, and Cr.[87] Besides the focus on the metal sites' activity, studying of Fe SMAs also provides interesting insights into the mechanism of the CO_2 reduction on metal sites embedded in carbon substrates. For example, Zhang et al. reported the atomic dispersion of Fe^{2+} on N-doped graphene (Fe/NG), with the Fe-pyridinic N_4 configuration.[40] DFT calculations revealed that when two graphitic N atoms are doped nearby the Fe-N_4 site, the energy barrier for *COOH decreases from 0.63 eV (only Fe–N_4 motif in graphene) to 0.29 eV, and the

CO adsorption energy decreases from 0.5 to 0.3 eV (**Figure 6**). This explains the higher activity of Fe/NG compared to that of the molecular FePc, since the former also contains graphitic N atoms that are not present in the latter, suggesting the synergistic effect of the Fe–N_4 moieties and N-doping on the graphene surface for ECR.

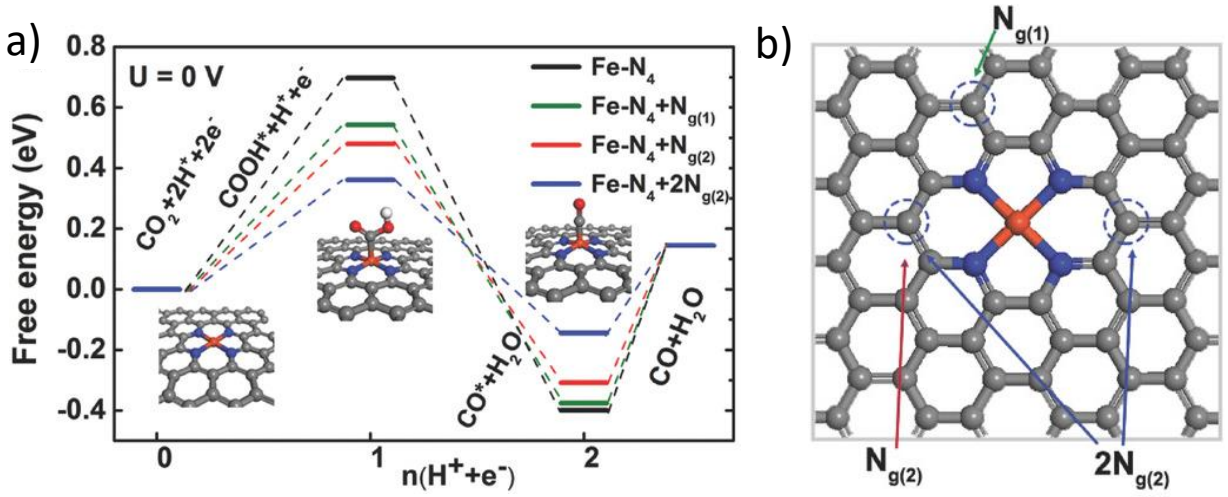

Figure 6. Theoretical calculations and proposed mechanism on the N-coordinated Fe catalytic site. a) Free energy diagram for electrochemical CO_2 reduction to CO on Fe–N_4 moieties embedded on graphene sheets; b) Top view of the optimized structures for Fe–N_4 moieties embedded on graphene layer and potential N-substitution. Reproduced with permission from reference [40]. Copyright 2018 Wiley.

3.1.4 Cu SMA catalysts

Similar to Cu metal, some Cu SMAs enable CO_2 electroreduction into products with more than 2-electron transfer; however, the low selectivity of the products has always been the main issue with these catalysts. The Cu-N_4 sites with pyridinic N atoms have been shown to catalyze the CO_2 reduction to methanol. For example, the catalyst which was prepared by Yang et al. containing N-doped through-hole carbon nanofibers (TCNFs) with dispersed Cu single atoms (CuSAs/TCNFs)[86] catalyzed the methanol formation with a maximal FE_{MeOH} of 44%; the other product is CO (FE_{CO} = 56%). This selectivity is similar to the one obtained with the Co SMA previously mentioned.[85] Interestingly, with less amount of through-holes, the catalyst's activity toward methanol decreased, suggesting that the holes in the carbon substrate adequately expose the Cu single atoms on the surface, allowing efficient diffusion of CO_2 to Cu active sites (**Figure 7**). The reason for the

production of MeOH on CuSAs/TCNFs, while other SMAs such as Ni mainly produce CO, was revealed by DFT calculations. The *COOH intermediate on the catalysts' surface can be converted into a *CO species, which can desorb to form CO in the case of Ni–N_4. For Cu–N_4, however, the CO desorption has a slightly positive free energy (0.12 eV), indicating an endergonic step. Therefore, the *CO intermediate on Cu–N_4 is not released from the surface and can be further reduced to methanol.

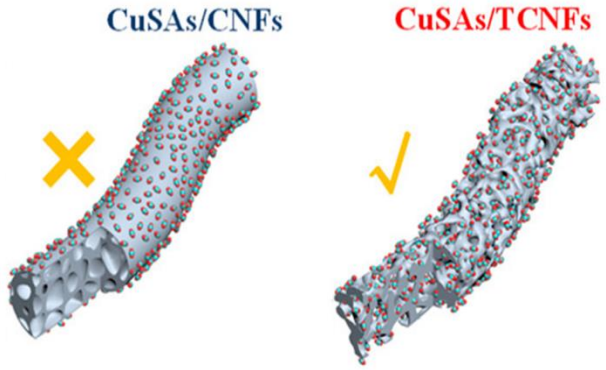

Figure 7. CuSAs/CNFs and CuSAs/TCNFs, the latter having through-holes. Reproduced with permission from reference [86]. Copyright 2019 American Chemical Society.

3.1.5. Other metals

Zn SMA catalysts for ECR are not as common as those based on previously mentioned transition metals. Nevertheless, a couple of Zn SMA catalysts have been reported for catalyzing the ECR to CO. Yang et al.[88] and Chen et al.[89] prepared Zn-coordinated N-doped graphene materials via the co-deposition method, with the majority of the Zn site in these materials being Zn-N_4. In both reports, CO was obtained with maximal FE_{CO} > 90%, but the current densities are only about few mA cm^{-2}, which are lower than those reported for other SMAs of Ni and Fe.[39, 59, 84]

Besides the transition-metal SMAs, some post-transition metals have also been investigated as catalysts for ECR, with the M-N_4 configuration also being observed in some cases. Zhang et al. prepared an N-doped carbon framework with dispersed Bi single atoms (Bi SAs/NC).[90] The CO_2 electroreduction activity of Bi SAs/NC is comparable to that of Zn SMAs when measured in a similar reaction condition. DFT calculations comparing Bi-N_4, Bi-C_4 and Bi moieties showed that the Bi-N_4 site has a much lower Gibbs free energy for *COOH formation, and a more positive $U_L(CO_2) - U_L(H_2)$ value than those of the latter two sites, indicating its higher activity and selectivity for CO_2 reduction to CO. A similar catalytic performance was also observed for a Sn-

based catalyst (AD-Sn/N-C1000) reported by Zhao et al.[91] It is worth noting that using Sn metal as a catalyst for ECR often results in the formic acid product; however, the single Sn atom catalyst in this work gives CO as the main product. This illustrates the drastic difference between metal catalysts in the bulk and the single-atom forms.

3.2. Effect of the coordination environment

3.2.1. N as coordination element

The coordination environment around the metal site in the N-doped carbon substrate is not always M-N_4 with four pyridinic N atoms, as discussed above. Other configurations such as M-N_xC_{4-x} or M-N_4 with a different type of N atom have been observed. These changes can significantly affect the activity, selectivity, and stability of the catalyst. Zhao et al. developed an electrocatalyst based on Ni single atoms distributed in N-doped porous carbon (Ni SAs/N-C), with the local structure of Ni fitted to a Ni-N_3C coordination environment.[76] The current density reaches a value of 10.48 mA cm^{-2} at -1.0 V vs. RHE, and the maximal FE_{CO} is 71.9%. These values are inferior to those obtained by Ni-N_4 sites,[39] exemplifying the sensitivity of the metal sites on their coordination environments.

An example showing the effect of coordination elements on the selectivity of products was demonstrated by Zu et al. The authors reported a catalyst based on atomically dispersed Sn atoms on N-doped graphene, with each Sn atom coordinated with two pyridinic N and two C atoms, i.e., Sn-N_2C_2 (**Figure 8a**).[92] Formate and H_2 were found as the main products in the liquid and gas phase, respectively, and the onset potential for the formate formation was quite low, with an overpotential of only 60 mV. Notably, compared to the Sn-N_4 sites reported by Zhao et al. mentioned above,[91] which produced CO, the Sn-N_2C_2 coordination environment favors a different product. This might be a topic for further investigation to understand the relation between the structure and product selectivity in these catalysts. The low onset potential was explained via DFT calculations, which illustrated that both the $*CO_2^{\bullet-}$ and $*HCOO^-$ formation processes for the $Sn^{\delta+}$ atom on N-doped graphene are exergonic, and the desorption of $*HCOO^-$ is the rate-limiting step (**Figure 8b**). The desorption energy with Sn-N-doped graphene is much smaller than that for Sn-graphene, which is expected from the effect of doping of N atoms since the presence of the stronger Sn-N bonds weakens the bond between Sn and $HCOO^-$, favoring the formate desorption at a low

overpotential. In addition, the calculated bond lengths of Sn-N and Sn-C within the Sn-N_2C_2 site were shorter than that of the Sn-C bonds in Sn-graphene, justifying the high stability of the catalyst.

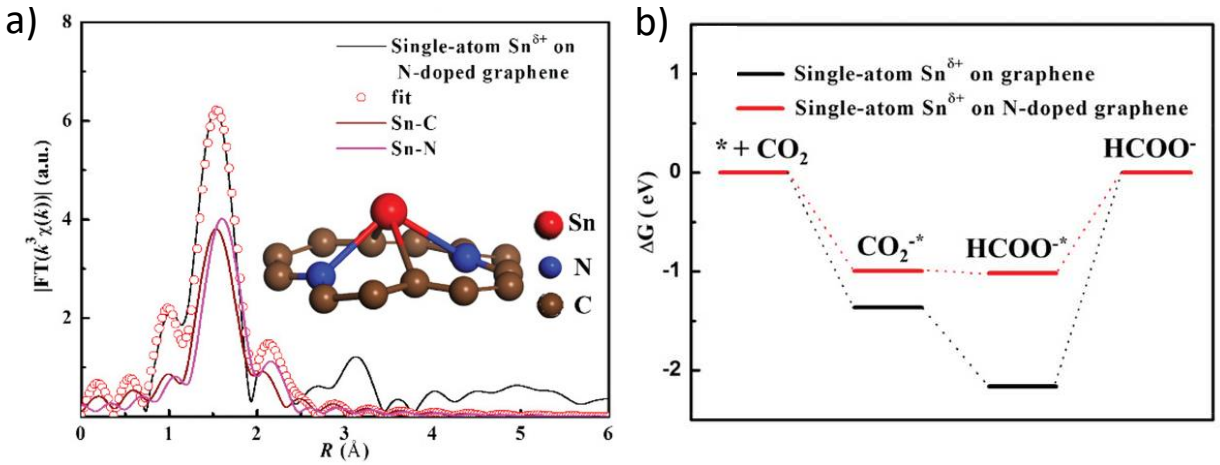

Figure 8. a) The fitting curve of k^3-weighted EXAFS spectra using the ARTEMIS module of IFEFFIT. Inset gives the corresponding atomic model, Sn (red), N (blue), and C (brown); b) Calculated free energy diagrams for CO_2 electroreduction to formate. Reproduced with permission from reference [92]. Copyright 2019 Wiley.

The three common configurations of N in N-doped graphene are pyridinic-N, pyrrolic-N, and graphitic-N, with their proportion varying on different materials depending on the synthetic conditions. Most previous works focused on metal-pyridinic N_4 sites; however, recent works have shown the advantages of having metal-pyrrolic N_4 sites, including the significant improvement of the catalyst's stability and the ability to obtain C_{2+} products, which were thought to be unlikely for SMAs. Gu et al. reported a catalyst (Fe–N–C) with dispersed single-atom Fe sites.[42] Different from the Fe-N_4 site reported by Zhang et al. mentioned above,[40] the Fe site in Fe-N-C has the +3 oxidation state (**Figure 9a**) and coordinated by four pyrrolic N atoms. CO was detected at a low onset potential of only 80 mV (–0.19 V vs. RHE), and with high selectivity of ~90%. The catalyst was found to be highly stable, even when tap water was used to prepare the electrolyte in place of deionized water. This high stability is in contrast to the quick degradation of the common Fe^{2+}-pyridinic N_4 sites, which was attributed to the pyrrolic type ligands in Fe^{3+}-N-C that are crucial to keeping the Fe sites in the +3 oxidation state during CO_2 reduction at moderate overpotentials (**Figure 9b**). Kinetics studies also revealed that for Fe^{3+}–N–C, the rate-limiting step is the protonation of the adsorbed CO_2^- to form an adsorbed *COOH intermediate and not the CO_2

adsorption as for other Fe^{2+} SMAs. The fast CO_2 adsorption in Fe^{3+}–N–C explains its low onset overpotential.

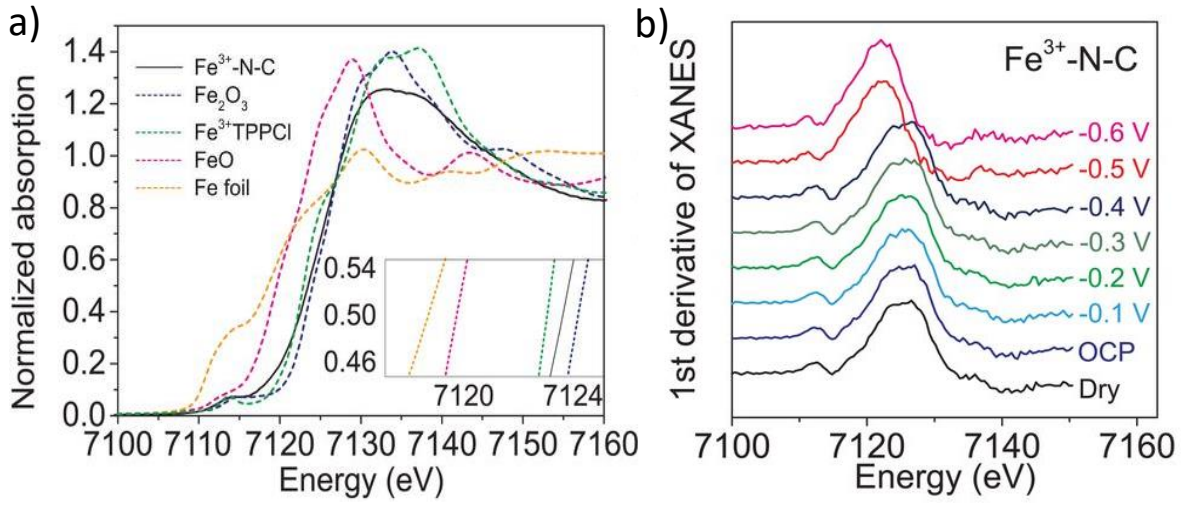

Figure 9. a) Fe K-edge XANES spectra of Fe^{3+}–N–C (black), Fe_2O_3 (blue dashed), Fe^{3+}TPPCl (green dashed), FeO (pink dashed), and Fe foil (orange dashed). (Inset) The enlargement of the main edges; b)The first derivative of the Fe K-edge XANES spectra of Fe^{3+}–N–C as dry powder (black) and loaded on glassy carbon electrodes at open circuit potential (OCP) (blue), –0.1 V (light blue), –0.2 V (green), –0.3 V (dark green), –0.4 V (dark blue), –0.5 V (red), and –0.6 V (pink) versus RHE. Reproduced with permission from reference [42]. Copyright 2019 Science.

Similar to the work by Gu et al.,[42] research on SMAs coordinated by pyrrolic N atoms for other metals is drawing great attention. Recently, Zhao et al. reported the atomic distribution of Cu on N-doped porous carbon (Cu-SA/NPC), with Cu species existed as Cu^{2+} coordinated by four pyrrolic N atoms.[93] This catalyst produced both liquid and gas products, including formic acid, acetic acid, methanol, ethanol, acetone, H_2, and CO. While the selectivity toward these products is low, acetone was obtained as the major product, with the $FE_{acetone}$ reaching a maximum value of 36.7%. The proposed mechanism for CO_2 reduction to acetone involves the following steps: $CO_2 \rightarrow *COOH \rightarrow *CO \rightarrow *COCO \rightarrow *COCOH \rightarrow *COC \rightarrow *COCH \rightarrow *COCH_2 \rightarrow *COCH_3 \rightarrow *COCOCH_3* \rightarrow *COHCOCH_3 \rightarrow *CCOCH_3 \rightarrow *CHCOCH_3 \rightarrow *CH_2COCH_3 \rightarrow CH_3COCH_3$ (**Figure 10a**). DFT calculations revealed that the reduction of CO_2 to acetone is thermodynamically favorable on the Cu-SA/NPC catalyst. The rate-limiting step is the activation of CO_2 to form a *COOH intermediate via a 1-electron transfer process, with the energy is much lower for the Cu-pyrrolic-

N_4 site than for the Cu-pyridinic-N_4 site. Interestingly, the calculations also showed that the *CO species could dimerize on a single atom Cu of the Cu-pyrrolic-N_4 site, but not on the Cu-pyridinic-N_4 site (1.67 V) (**Figure 10b**), indicating the superiority of the Cu-pyrrolic-N_4 site for CO_2 reduction to C_{2+} products.

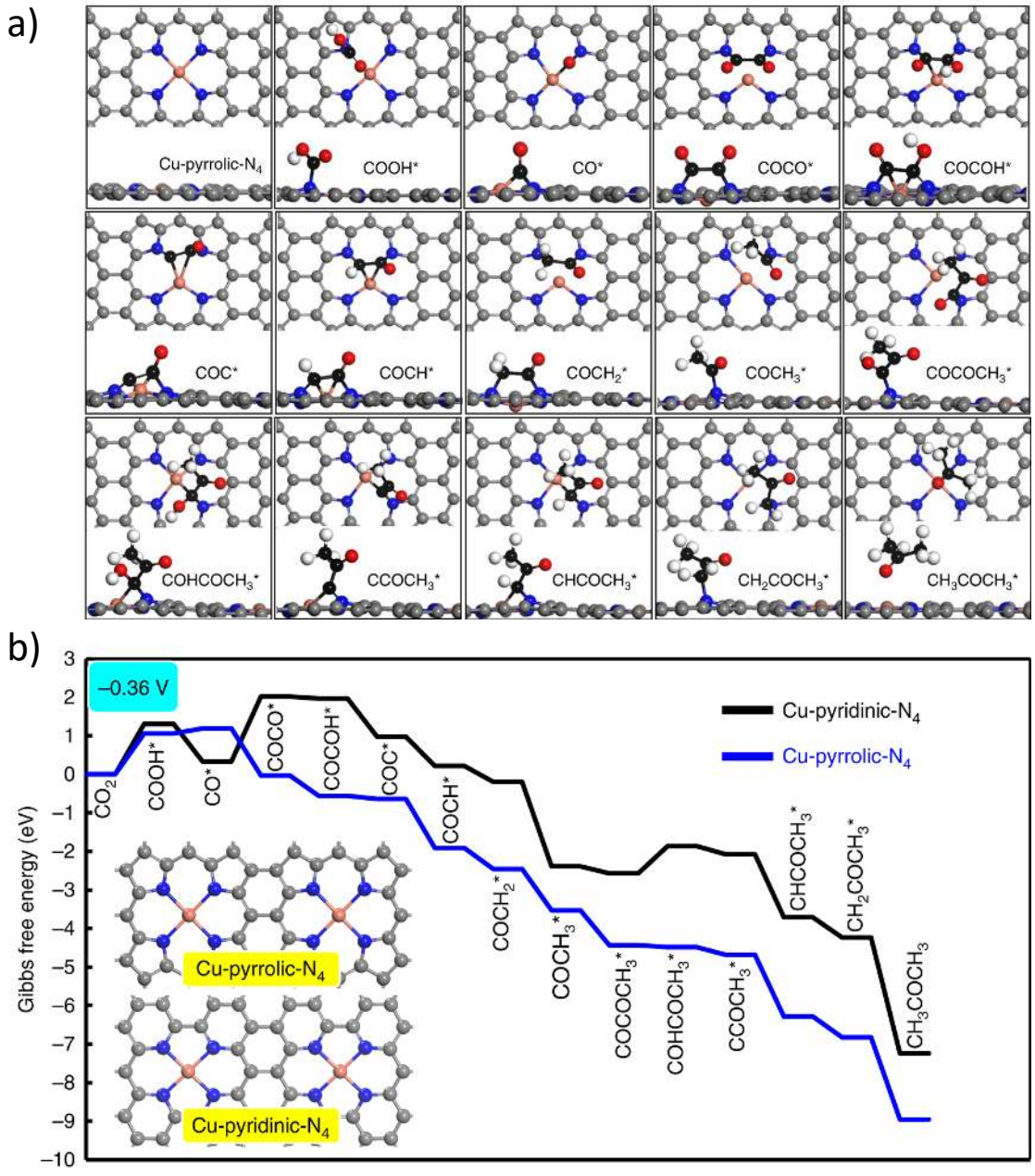

Figure 10. a) Optimized structures of all reaction intermediates involved in the pathways of CO_2 reduction on the Cu-pyrrolic-N_4 site (gray: C of catalyst; black: C of adsorbate; red: O;

orange: Cu; blue: N; white: H); b) Free energy diagrams calculated at a potential of −0.36 V for CO_2 reduction to CH_3COCH_3 on Cu-pyridinic-N_4 and Cu-pyrrolic-N_4 sites of Cu-SA/NPC. Inset: the computational models. Reproduced with permission from reference [93]. Copyright 2020 Nature.

It is worth noting that a family of Fe, Co, Ni, and Cu SMAs coordinated by four pyrrolic N atoms have been recently reported by Wanzhen et al.[94] They were prepared via the pyrolysis of the corresponding metalloporphyrin molecules with a polymer originated from the self-assembly of melamine and cyanuric acid. Different from the above-mentioned work by Zhao et al.[93], in which the Cu-pyrrolic N_4 sites were prepared via the ZIF-8 template, the Cu and the other catalysts in this work only catalyzed the CO_2-to-CO conversion. The Ni analog showed the highest activity and selectivity although its performance was not improved compared to that of the Ni SMAs with pyridine N atoms.[39, 59, 84] The selectivity toward CO in this work indicates that the preparation method of SMAs is critical to tune the products.

3.2.2. O, S, and halide as coordination elements

The presence of other heteroatoms besides N, such as O, S, and halides, is another approach that has been used to improve the activity, selectivity, and stability of SMAs. For example, Jeong et al. reported Ni SMAs on reduced graphene oxide (Ni-N-RGO).[95] The Ni single atoms were coordinated by four N atoms and one axial oxygen ligand, i.e., Ni-N_4O. This catalyst displayed high selectivity for CO production, with FE_{CO} reached 97%, and a maximal total current density of 42 mA cm^{-2} at -1.0 V vs. RHE. This performance is superior to those for Ni^{2+}@NG and Ni-N_4-C with Ni-N_4 sites previously mentioned.[39, 59] However, it is unclear why the presence of an axial oxygen ligand results in such enhanced activity.

The catalytic activity enhancement by introducing S into the coordination environment was observed by Yang et al., who prepared single-Ni-atom catalysts, A-Ni-NG and A-Ni-NSG, in which the Ni sites display Ni–N_4 and Ni–N_3S structures, respectively.[96] The CO_2 reduction onset potential of A-Ni-NSG was around 100 mV lower than that of A-Ni-NG, which was attributed to the non-centrosymmetric environment around the Ni atoms, promoting better adsorption of reactants and intermediates on the catalyst surface. Notably, the oxidation state of the Ni atoms in both A-Ni-NG and A-Ni-NSG is +1, which is rarely observed and different from the +2 oxidation state in other Ni single-atom catalysts. The strong interaction between the Ni^+ sites and CO_2,

manifesting as the charge transfer from Ni^+ to the carbon 2*p* orbital in CO_2 to form a $CO_2^{\delta-}$ species (**Figure 11**), led to the enhanced catalytic performance of both A-Ni-NG and A-Ni-NSG for CO production. These catalysts exhibited current densities of ~90-110 mA cm^{-2} compared to current densities of 20-30 mA cm^{-2} displayed by other Ni-based SMAs.[39, 59, 84]

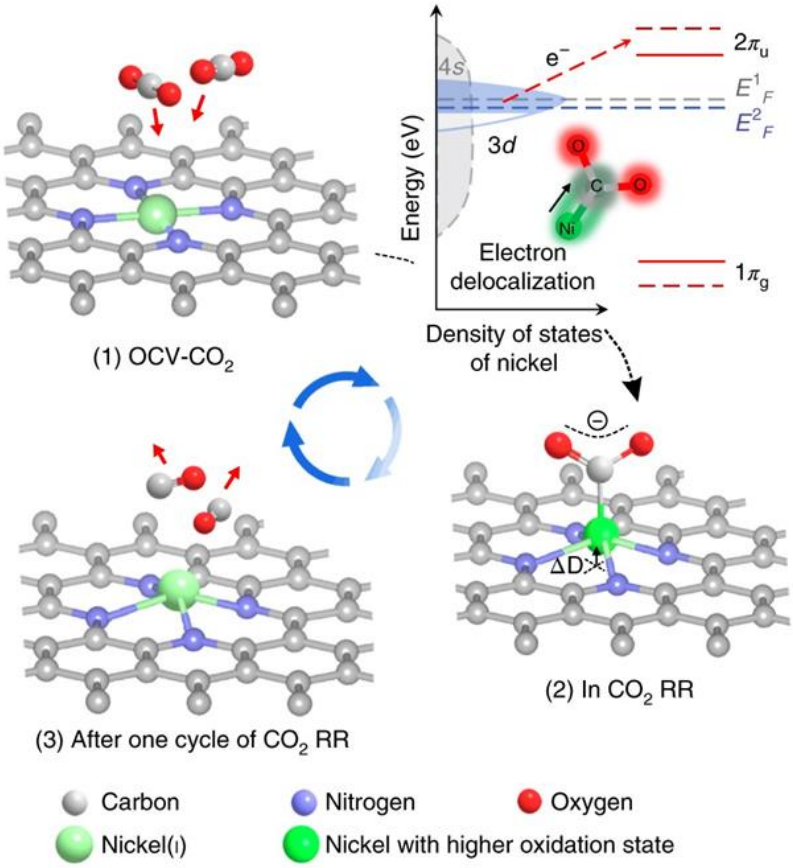

Figure 11. The displacement of Ni atom out of plane resulting from electron transfer from Ni atom to CO_2. The upper-right schematic shows the activation processes for CO_2 molecules on the Ni^+ site. A valence band structure, similar to metallic nickel, was used to simplify the schematic illustration. The red arrow represents the electron transfer from the Ni^+ to adsorbed CO_2. E^1_F and E^2_F are Fermi levels of A-Ni-NG before and after the formation of Ni-$CO_2^{\delta-}$, respectively. $1\pi_g$ and $2\pi_u$ are CO_2 molecular orbitals. Reproduced with permission from reference [96]. Copyright 2018 Nature.

The presence of heteroatoms in the coordination environment of the metal sites can enhance the catalytic performance of the catalyst, but this effect is not universal and depends on the nature

of the metal. Zhang et al. prepared a Mn-based catalyst ((Cl, N)-Mn/G) in which each Mn atom was coordinated with one Cl atom and four N atoms, i.e., Mn-N_4Cl.[43] The CO production by ((Cl, N)-Mn/G) was significantly better than that for Cl-free N-Mn/G (**Figure 12a, b**). The author also prepared (Cl, N)-Fe/G and (Cl, N)-Co/G and found that the electrocatalytic activities of these analogs were lower than that of (Cl, N)-Mn/G, suggesting that the effect of Cl coordination is less significant for Co and Fe. XANES studies on (Cl, N)-Mn/G showed that the oxidation state of the Mn sites was increased (**Figure 12c**) upon exposure to CO_2, which was attributed to the charge transfer from Mn to the carbon 2*p* orbital in CO_2 to form a $CO_2^{\delta-}$ species. During the CO_2 reduction process, the Mn K-edge shifted back to lower energy that was even lower than that of the original (Cl, N)-Mn/G catalyst (**Figure 12c**), and the Mn-Cl bond was enlarged, suggesting that the Mn is positioned in the N_4 plane after CO_2 binding. The release of CO allowed the Mn sites to return to the original configuration (**Figure 12d**). The coordination of Cl and the out-of-plane Mn atoms are critical to promote the adsorption of CO_2 and intermediate species on the catalyst surface, stabilize the low-energy transition state, and facilitate the product desorption.

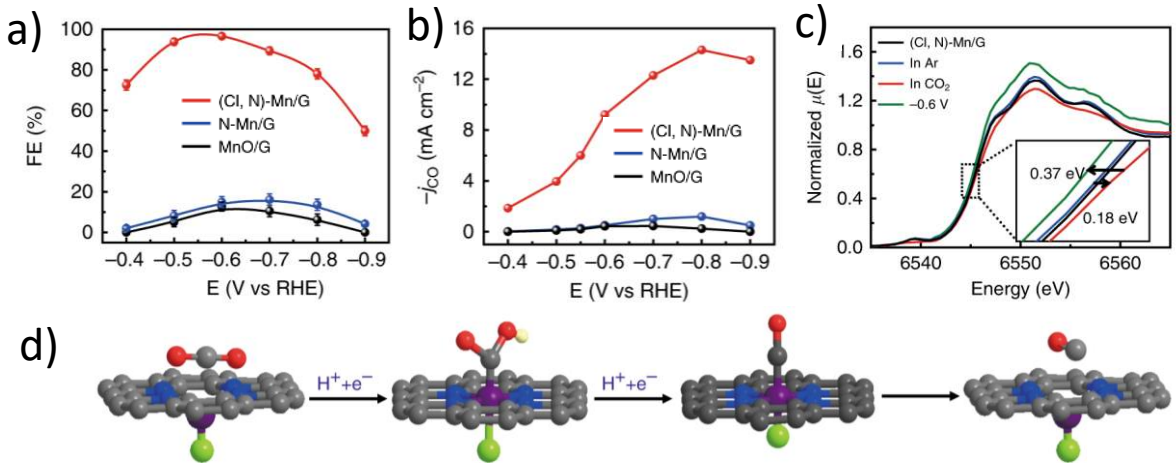

Figure 12. a) FE_{CO} at various applied potentials; b) Potential-dependent CO partial current density; c) Normalized XANES of (Cl, N)-Mn/G catalyst under various conditions (inset is the magnified image); d) Structural evolution of the active site for (Cl, N)-Mn/G in electrochemical CO_2RR (Mn: purple, Cl: green, N: blue, O: red, H: white and C: gray). Reproduced with permission from reference [43]. Copyright 2019 Nature.

Most SMAs are incorporated into carbon-based materials, while metal oxide substrates are rarely employed. Nevertheless, it is interesting to investigate the catalytic performance of SMAs

for ECR with an M-O_n configuration. Wang et al. reported a catalyst (Cu-CeO_2) with single-atom Cu ions doped on Ceria (CeO_2).[97] This catalyst produced a wide range of products, including CH_4, C_2H_2, CH_3COOH, C_2H_5OH, CH_3OH, CO, HCOOH, and H_2, with their molar ratios strongly dependent on the loading amount of Cu. The optimized sample with 4 wt% Cu loading (Cu-CeO_2-4%) produced CH_4 as the main product (58%); however, this performance was only stable for up to ~2 hours of electrolysis. Apparently, there is a need to improve the selectivity and stability of these M-O_n catalysts.

3.2.3. Coordination number

The coordination number of the metal ion can affect its catalytic activity. This effect can be subtle or significant, depending on the nature of the SMA. Cheng et al. employed a defect-rich microwave exfoliated graphene oxide (MEGO) as the precursor to atomically disperse Ni single atoms on N-doped graphene (Ni-N-MEGO).[98] The Ni coordination environment was a combination of unsaturated Ni-N_2, Ni-N_3, and Ni-N_4 species. The current density and FE for CO are similar to those of Ni−N_4 catalysts abovementioned,[39, 59] indicating that the presence of unsaturated Ni-N_2 and Ni-N_3 species is not a decisive factor in the catalytic activity of Ni SMAs.

The change in the coordination number showing enhanced catalytic performance has been observed in Co SMAs. Pan et al. reported the atomically dispersed Co sites (CoPc) anchored on polymer-derived hollow N-doped porous carbon spheres (HNPCSs).[99] The N atoms on the surface of the HNPCSs establish a dative bond with the Co atom of CoPc; thus, the Co site has a Co-N_5 coordination environment. The CO current density was around 15 times higher than that of the molecular CoPc. The authors also prepared Co−N_4/HNPCSs and Co−N_3/HNPCSs and found that the FE_{CO} for these catalysts with lower coordination numbers slightly decreased. It was not clear why the selectivity for CO drops with the decrease of Co−N_x coordination in this case, which might be the topic for further investigation.

Wang et al. also studied the effect of changing the coordination number around the single Co atom on the catalytic activity. Opposite to what overserved by Pan et al.[99], they suggested that the decreased coordinating N results in more unoccupied 3d orbitals of Co atoms, which might facilitate the adsorption of the intermediates.[45] The authors prepared Co-based catalysts in which the coordination environment around the Co site changed from Co-N_4 to Co-N_3 and Co-N_2 (**Figure 13a**). When tested for CO_2 reduction, Co-N_2 exhibited a much higher catalytic activity and

selectivity compared to that of Co-N_3 and Co-N_4. The higher activity of Co-N_2 was supported by its lowest charge transfer resistance among the three catalysts and the less endergonic formation of $CO_2^{\bullet}$-* (**Figure 13b**). Interestingly, even with low coordination, the Co-N_2 sites were shown to be stable for at least 60 hours of electrolysis.

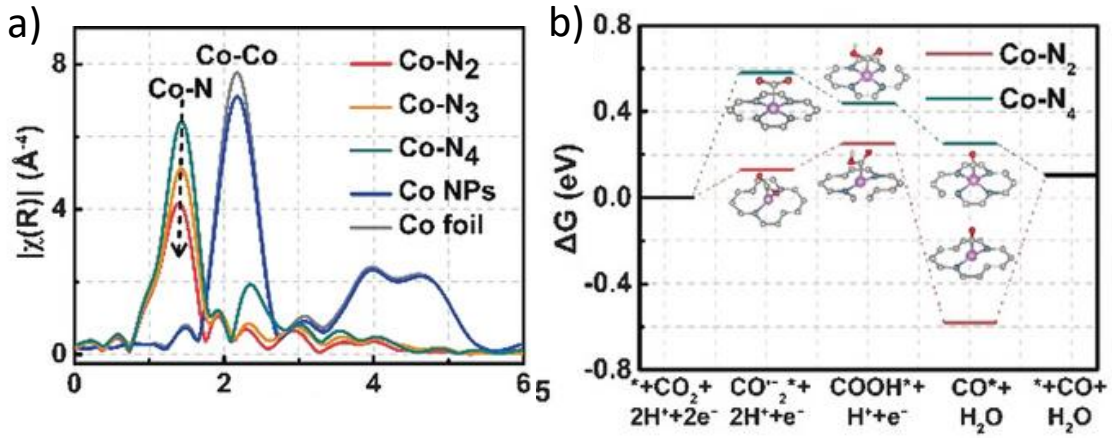

Figure 13. a) EXAFS spectra confirm the atomic dispersion of Co atoms in Co-N_2, Co-N_3, and Co-N_4, and also suggest the lowest N coordination number in Co-N_2; b) Calculated Gibbs free energy diagrams for CO_2 electroreduction to CO on Co-N_2 and Co-N_4. Reproduced with permission from reference [45]. Copyright 2018 Wiley.

4. Electrochemical CO_2 reduction mechanism on SMA catalysts

4.1. General overview of reaction mechanisms for the ECR

The reaction mechanism for the ECR is intensively studied during the last decades either through in-situ spectroscopic means (e.g., in-situ Raman and IR) [100-109] or computational methods based on the DFT[7, 37, 98, 110-119] While there is still a distinct lack of consensus among researchers in this field about some of the reaction steps, key reaction intermediates such as adsorbed CO (*CO) are generally believed to be of deterministic role in the reaction pathway. In CO_2 reduction to multi-carbon (C_{2+}) hydrocarbon, carbon-carbon (C-C) coupling is the most crucial step among three possible bond formations i.e., C-C coupling, O-H, and C-H hydrogenation bond formations. On the one hand, different mechanisms are proposed for the C-C bond formation, including *CO dimerization (i.e., *OCCO formation), *CO coupling with hydrogenated *CO such as *CHO and *COH (i.e., *OCCOH or *OCCHO formation), coupling of hydrogenated *CO (i.e., *HOCCOH formation), or coupling of deoxygenated carbonaceous intermediates such as *C, *CH or *CH_2 to

form *CC, *HCCH, or *H_2CCH_2. By and large, the C-C coupling step is the most discussed and yet controversial step in the proposed mechanisms for the ECR. Hydrogenation steps (O-H and C-H bonds formation) are well categorized into two mechanisms [120]: the Eley–Rideal mechanism, in which water molecule and electron are the reactants to provide the hydrogen; and the Langmuir–Hinshelwood mechanism, in which catalyst surface adsorbed hydrogen (*H) is the reactant. Therefore, the Langmuir-Hinshelwood mechanism requires additional catalytic active site for the *H. This active site needs to be adjacent to the main active site that adsorbs the intermediate to form the hydrogen bond (*C-H or *O-H). In contrast, in the Eley-Rideal mechanism, hydrogen is provided through the bulk electrolyte, and there is no need for the additional catalytic active site. This fact is of particular importance in SMA catalysts.

In most reaction mechanism perspectives, reaction pathways are split into C_1 and C_{2+} pathways, in which the former is divided into CO and formate pathways, while the latter one goes mainly through *CO intermediate and the subsequent C-C coupling.[9] It is mostly agreed that formate formation is through the *HCOO intermediate —i.e., one of the two possible intermediates after CO_2 first hydrogenation— and is bound to the surface of the catalyst via both oxygen atoms. Therefore, formate formation most likely requires two adjacent active sites with similar intrinsic (catalytic) properties for oxygen adsorption. This fact might be a limiting factor in SMA catalysts where there is only one single atom surrounded by coordination atoms of a quite different nature. Thus, on those SMA catalysts that produce formate, the configuration of *CHOO intermediate on the catalyst surface might be quite different than that on regular catalysts. In addition, on regular catalysts it is documented that the electrolyte pH regulates the availability and source of hydrogen for the first hydrogenation step.[121] It is shown that surface hydrogen is favored compared to the proton (H^+) available in the electrolyte —mainly due to the polarity differences in the C-H bond and the O-H bond— [122] which further limits the capability of SMA catalysts for formate formation.

CO formation, on the other hand, is shown to be through the carboxyl intermediate (*COOH), which is formed via a proton coupled electron transfer (PCET) mechanism.[123] This intermediate is bonded to the catalyst surface via the C atom. Further dehydrogenation of this species leads to *CO formation, which can desorb from the surface or undergo further reductions, depending on its adsorption energy on the catalyst. The adsorption energy of *CO on different metal catalysts is well correlated to the catalytic activity of these catalysts through the scaling relations.[124] These

scaling relations demonstrate, for instance, that *CO is so strongly adsorbed on Ni and Pt that poisons the active sites and results in HER as the main reduction reaction product. On the other end of the spectrum, *CO is loosely adsorbed on Ag and Au and leaves the surface upon formation, and CO is observed as the main product of the ECR on these metals. In between, metals like Cu adsorb *CO neither too strongly nor too loosely to let it undergo further reduction. The main question is what happens to these scaling relations when they are examined on SMA catalysts? Due to the change in the electronic structure of the active sites because of their undercoordinated feature and surrounding coordination atoms, different adsorption energies and scaling relations are expected for SMA catalysts. Distinct electronic structure of SMA catalysts, thus, significantly changes the reaction energetics of the ECR if not the reaction mechanism. In the following sections, it is shown that despite the fact that SMA catalysts share similar pathways with their regular counterpart bulk metals for the ECR products, they demonstrate quite different catalytic activity, selectivity, and even stability. For instance, bulk metals such as Ni, Pt, and Fe generate H_2 under the ECR condition due to their poor activity for the ECR,[125] however as SMA catalysts hydrogen production is significantly suppressed and instead CO is generated along with formate, methane, and methanol. As another example, Cu is considered as a unique catalyst for C_{2+} hydrocarbon production;[9, 126] however, C_{2+} products are rarely observed on Cu SMA catalysts. Here we discuss: why the HER is significantly suppressed on SMA catalysts compared to their regular counterparts; why CO is the ECR's major product in most of SMA catalysts; why producing C_{2+} products are difficult on SMA catalysts; and why methanol is produced in a considerable amount on some of SMA catalysts.

4.2. Suppression of the HER on SMA catalysts

While HER is a competing side reaction in the ECR and several metal catalysts such as Ni, Fe, and Co produce mostly H_2 under the ECR condition, SMA catalysts behave differently and hydrogen production is significantly suppressed. There are two mechanisms for the HER: the Volmer-Tafel and the Volmer-Heyrovsky mechanisms.[127] The very first step of the HER is the Volmer reaction, through which, a proton (from the electrolyte) and an electron (provided through the catalyst) react (i.e., PCET mechanism), and consequently, the adsorbed hydrogen on the surface (*H) is formed. The second step can proceed through either the Heyrovsky reaction or the Tafel reaction. The former reaction is another PCET step, through which the adsorbed *H directly

reacts with a solvated proton from the electrolyte and an electron from the catalyst to generate $H_2(g)$. The latter reaction, however, requires that the proton and electron generate a new adsorbed hydrogen (*H), and then two adsorbed hydrogens undergo a coupling step to form $H_2(g)$.

$$^*H + H^+ + e^- \xrightarrow{Heyrovsky} H_2(g)$$

$$^*H + H^+ + e^- \longrightarrow 2^*H \xrightarrow{Tafel} H_2\ (g)$$

Skúlason and coworkers [128] performed DFT computations to study the HER on different bulk metal catalysts and realized that the Tafel reaction is much more favorable than the Heyrovsky reaction. They showed that the activation energy for the HER at zero applied bias (ΔE = 0) on Pt (111), for instance, is 0.55 eV for the Tafel reaction (**Figure 14a**), while it is almost two times larger (1.03 eV) for the Heyrovsky reaction (**Figure 14b**). Authors also investigated other metals such as Au, Cu, Ni, Pt, and Co, and concluded that the Volmer-Tafel is the leading mechanism for the HER on these catalysts, with the Tafel reaction as the rate-limiting step. [128] Since the Tafel mechanism requires at least two adjacent active sites for the *H adsorption to occur, it will be automatically precluded on SMA catalysts. Therefore, the Volmer-Heyrovsky mechanism with a much higher activation energy barrier is the dominant reaction pathway for the hydrogen formation on SMA catalysts, and thus, the HER is considerably suppressed on these catalysts compared to their bulk metal counterparts.

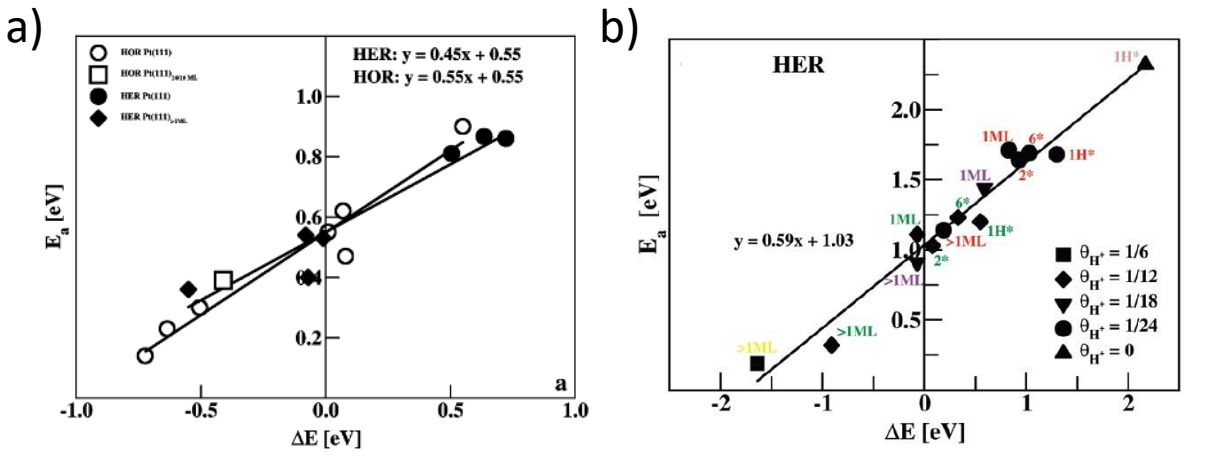

Figure 14. a) Activation barrier, E_a, for HER on Pt(111) via the Tafel reaction as a function of the reaction energy, ΔE. X=0.02; b) Activation barrier, E_a, for the HER on Pt (111) via the Heyrovsky

reaction as a function of the reaction energy, ΔE. X=0.15. Reproduced with permission from reference [128]. Copyright 2010 American Chemical Society.

Similar rationale can be applied to the ECR first hydrogenation step. Both Tafel-like or Heyrovsky-like steps can exist for CO_2 hydrogenation to form *COOH. However, the Heyrovsky-like mechanism deems to be more plausible on SMA catalysts.[127]

$$CO_2 + {}^*H \xrightarrow{Tafel} COOH^* + {}^*H \xrightarrow{Tafel} CO(g)$$

$$CO_2 + H^+ + e^- \xrightarrow{Heyrovsky} {}^*COOH + H^+ + e^- \xrightarrow{Heyrovsky} CO(g)$$

Computational studies [127] have assessed these two mechanisms on bulk Fe and its porphyrin-like counterpart SMA catalyst. For the porphyrin-like structure, the Volmer-Heyrovsky mechanism is the leading mechanism, while for the metal catalyst, Volmer-Tafel, which is also a more favorable mechanism for the HER, proceeds the reaction pathway (**Figure 15**). Therefore, the HER is significantly suppressed on the SMA catalyst of Fe.

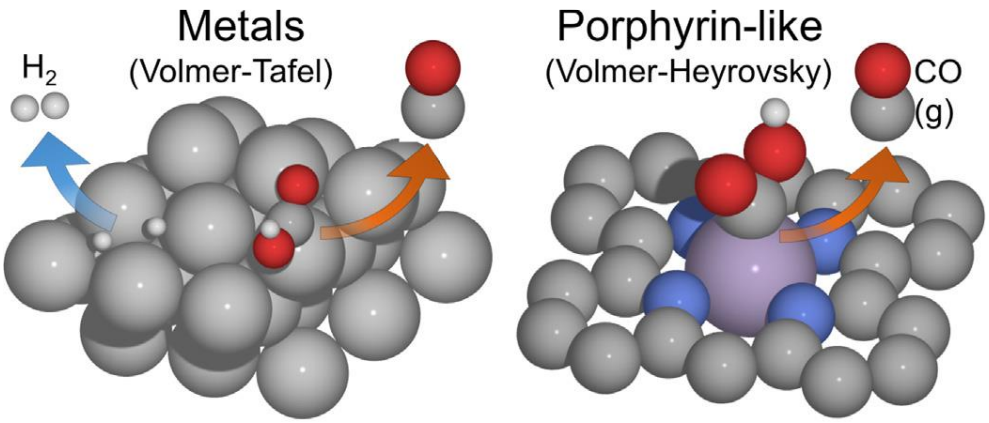

Figure 15. Illustration of a metal surface (left) and a porphyrin-like structure (right). On the metal, the HER can run via a Volmer–Tafel mechanism, while the porphyrin-like structure forces HER or ECR to run as a Volmer–Heyrovsky mechanism. Reproduced with permission from reference [127]. Copyright 2017 Elsevier.

4.3. Suppression of C_{2+} products formation on SMA catalysts

There is a common consensus that SMA catalysts are unable to produce C_{2+} products because generating those products requires the dimerization of two or more C-based intermediates such as *CO, *CHO, *COH, or *CH_x.[119, 129-130] In SMA catalysts, however, the metal atoms exist as

atomically dispersed sites, and hence the interaction of two or more C_1 intermediates is not plausible. Therefore, as for the HER, C_{2+} product formation is expected to be suppressed on SMA catalysts, mainly due to the large diffusion energy barrier for the intermediates on active sites far from each other. Notwithstanding, a very recent paper published by Zhao et al. reported that multi-carbon products are achievable on SMA catalysts.[93] Nevertheless, most experimental results confirm that SMA catalysts (even Cu SMA) are not as capable as regular catalysts to generate C_{2+} products.

4.4. Scaling relation and CO formation on SMA catalysts

Scaling relations, i.e., linear correlations between Gibbs energies (or in some cases adsorption/binding energies) of two reaction intermediates of the ECR,[124, 131-132] have been guiding to understand the mechanism and limits of a reaction, as well as to predict the catalytic performance of metals in high throughput analyses. Scaling relations, however, are mostly developed for pure metal catalysts. The general aim is to break the scaling rules and develop catalysts that go beyond the limitations imposed by these relations. For instance, it is of great interest to change the binding energy of a specific intermediate while keeping those of others intact, and thereby steer the reaction toward the desired product. But, breaking the scaling relation is not an easy and straight-forward task.[132]

SMA catalysts possess a very distinct atomic environment and so a different electronic structure compared to their regular metal catalyst counterparts. Back et al. [133] demonstrated that single (transition-) metal atoms such as Co, Fe, Cu, Ni, and Ir supported on TiC are capable of breaking such a scaling relation. They calculated the limiting potential (U_l) on M and M@d-TiC (M stands for the transition metal) for the ECR, and observed that for the pure metal catalysts either the first activation step ($CO_2 + H^+ + e^- \rightarrow *COOH$) or the protonation of the *CO intermediate ($*CO + H^+ + e^- \rightarrow *CHO/*COH$) is the potential determining step (PDS). However, in contrast, the PDS on the M@d-TiC is one of the following steps:

(i) $*COOH + H^+ + e^- \rightarrow *CO + H_2O$

(ii) $*CHOH + H^+ + e^- \rightarrow *CH + H_2O$

(iii) $*CHO + H^+ + e^- \rightarrow *CHOH$

(iv) $*CH + H^+ + e^- \rightarrow *CH_2$

Theoretical limiting potential (U_l) for different M@d-TiC(100) is shown in **Figure 16a**.

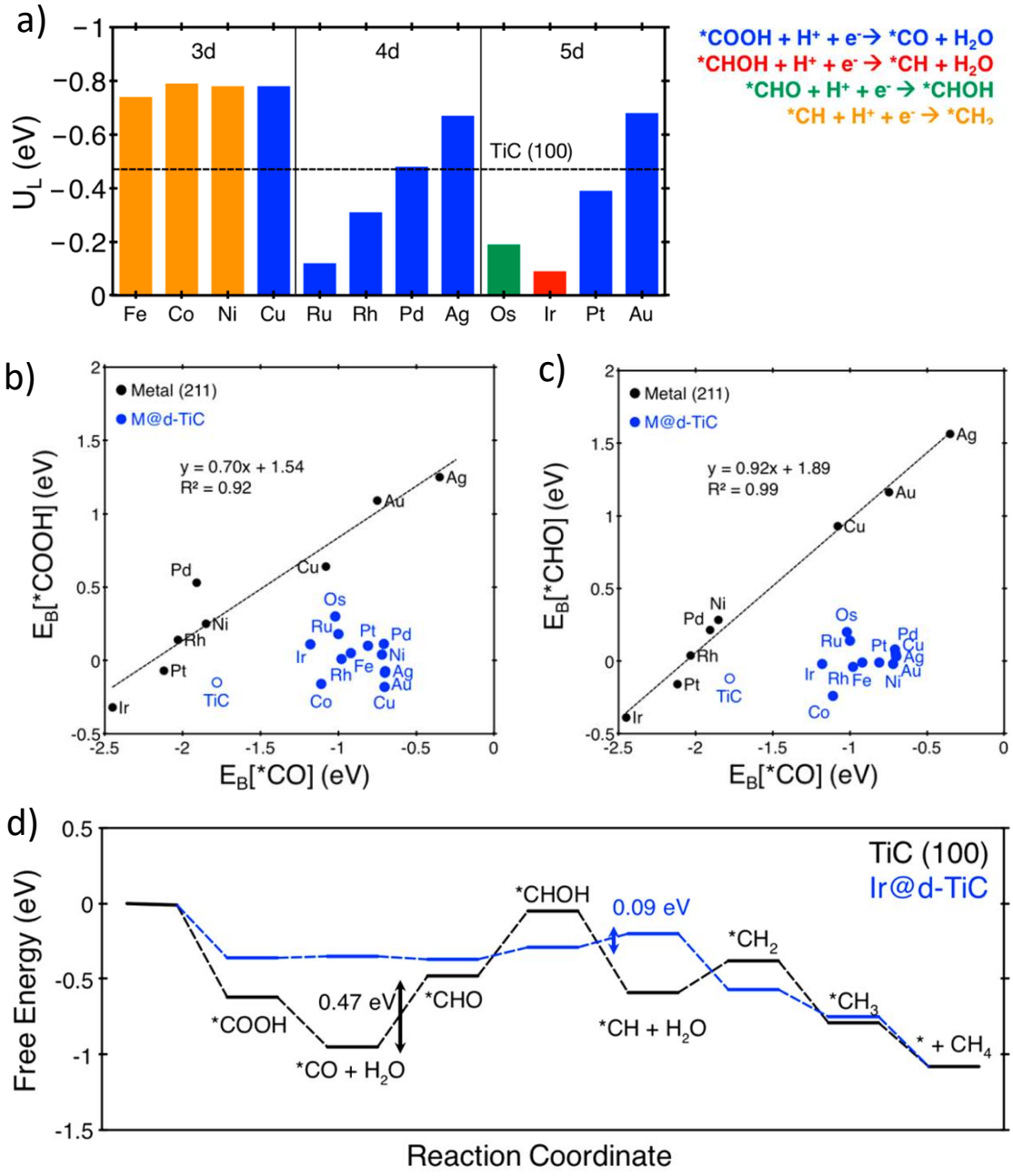

Figure 16. a) Theoretical limiting potential (U_l) for different M@d-TiC(100); b) *COOH; and c) *CHO binding energies plotted as a function of *CO binding energy for transition-metal (211) surfaces (black) and M@d-TiC (blue); d) Free-energy profiles for CO_2 reduction reaction at 0 V vs. RHE on TiC (black) and Ir@d-TiC (blue). PDS and corresponding free energy change are

shown. Reproduced with permission from reference [133]. Copyright 2017 American Chemical Society.

As seen in **Figure 16a**, Ir@d-TiC has an extraordinarily low U_l which makes it an ideal catalyst for the ECR. To investigate the origin of such an activity, the scaling relation of binding energy of two important, determining intermediates of the ECR, that is, *COOH and *CHO was plotted vs. *CO (**Figure 16b, c**). The data revealed that M@d-TiC breaks the scaling relation, and the binding energies of *COOH and *CHO are uncorrelated with that of *CO. For most SMA catalysts (except Ag and Au), the binding energies of *CO decreased (i.e., became less negative) in comparison to those on pure metal catalysts and approached the binding energy of the pure Cu catalyst.[134] Therefore, *CO intermediate on Ir@d-TiC compared to Ir or TiC, for instance, was so destabilized that its protonation is not the PDS anymore (**Figure 16d**). Authors ascribed the weakened binding of *CO to the noticeably different electronic structure of pure metals catalysts and M@d-TiC ones.

According to the density of states of TiC, Ir(111), and Ir@d-TiC with adsorbed CO, it is concluded that for both bare TiC and pure Ir(111), there are two localized energy states owing to the interaction between C(p_z) of TiC and C(p_z) of *CO (denoted as (*i*) and (*iii*) in **Figure 17a, b**). There is also one localized energy state originated from the interaction between C(p_x, p_y) of TiC and C(p_x, p_y) of *CO (denoted as (*ii*) in **Figure 17a, b**). On Ir@d-TiC, by contrast, there is one localized energy state arising from the interaction between Ir(d_{z^2}) and C(p_z) of *CO, and one from the interaction between Ir(d_{xz}, d_{yz}) and C(p_x, p_y) of *CO (**Figure 17c**). Therefore, the lack of (*i*) type interaction between the Ir@d-TiC catalyst and the *CO intermediate is responsible for the weakened binding, thereby leading to a considerably low limiting potential.[133]

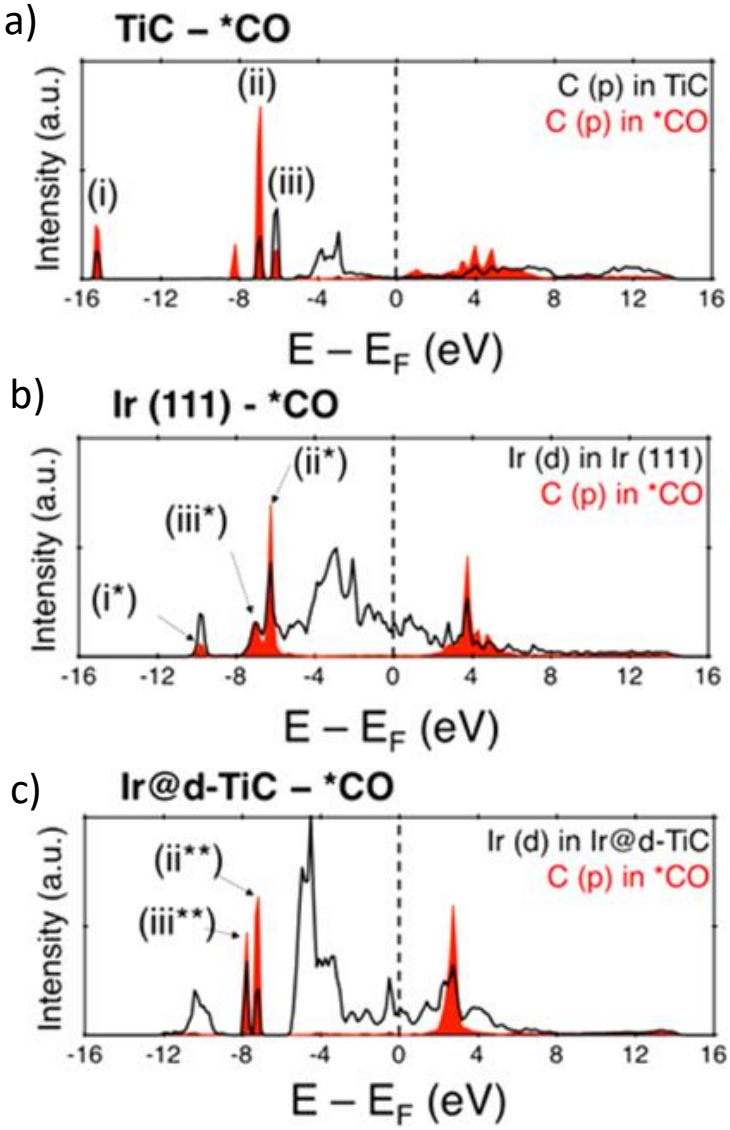

Figure 17. Density of states (DOS) of (a) TiC; (b) Ir(111); and (c) Ir@d-TiC interacting with *CO. The *CO binds to the surface C for TiC but to Ir for Ir@d-TiC. We note that (ii), (ii*), and (ii**) denote the equivalent bonding orbital, and similarly so for (iii), (iii*), and (iii**). Reproduced with permission from reference [133]. Copyright 2017 American Chemical Society.

Back et al. [130] also performed a series of DFT computations for SMA catalysts of transition metals supported on graphene with single and double vacancies. Most of the selected transition metals were found to bind strongly enough to the graphene surface with single and double vacancies. Therefore, no nanoclusters from metal atom aggregation would be expected. The fact that single atoms remain intact and stable on the support is a potential explanation for the relatively

high stability of SMA catalysts under the ECR condition. Using limiting potential criteria, the authors concluded that Ni and Pt single atom catalysts at double vacancy are the best performing ones for CH_3OH production, while Os and Ru single metal atoms at double vacancy show the best activities toward CH_4 formation. It is noteworthy that both Ni and Pt, as regular metal catalysts, generate almost exclusively H_2 under the ECR. According to the reaction free energy diagram, the authors observed that reaction intermediates are more stable on Pt (211) than Pt@dv-Gr (**Figure 18a**); however, the difference between *CO binding energies on these two catalysts (i.e., 0.98 eV) was the most considerable one, and that made Pt@dv-Gr had a noticeable lower limiting potential. This difference is mainly attributed to the atomic ensemble and the resulting electronic structure. [130] Optimized geometries of adsorbed CO on Pt (211) and Pt@dv-Gr revealed that the carbon atom of *CO intermediate bonds with two Pt atoms on Pt (211) (i.e., bridge site) that makes *CO particularly stable with large binding energy (**Figure 18c**). However, the *CHO intermediate bonds only with a single Pt atom on the surface (i.e., on-top site). As a result, converting *CO into *CHO requires considerable energy to overcome. In contrast, on Pt@dv-Gr, thanks to the lack of two Pt neighboring atoms, *CO could only bond with a Pt atom (i.e., on-top site) analogous to its protonated product, *CHO. Therefore, *CO on Pt@dv-Gr exhibits a more positive free energy, leading to a smaller energy barrier, and consequently, better performance as a catalyst for the ECR.

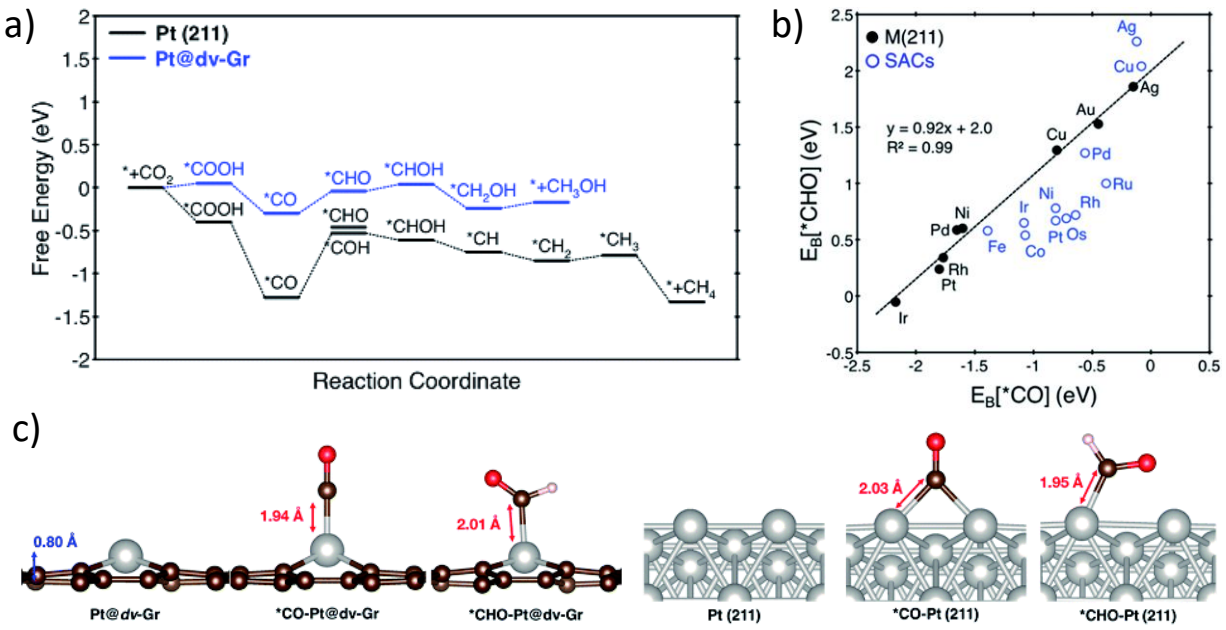

Figure 18. a) Reaction free energy diagram for the ECR to CH_4 and CH_3OH on Pt (211) and Pt@dv-Gr, respectively, at zero applied voltage (vs. RHE); b) Correlation between E_b[*CO] and E_B[*CHO] for transition metal (211) surfaces (black) vs. SACs (blue); c) Optimized geometries of Pt@dv-Gr and Pt (211) before and after adsorption of *CO and *CHO. Reproduced with permission from reference [130]. Copyright 2017 Royal Society of Chemistry.

Binding energies of *CO and *CHO adsorbed on regular transition metal catalysts are linearly correlated; however, they diverge from the correlation line for the SMA counterparts (**Figure 18b**). The authors found out that the electronic structure of the single atom played a paramount role in such a difference. As seen in **Figure 18b**, Ag and Cu reveal a positive deviation from the trend line, while other SMAs (e.g., Pt) show a negative deviation. According to the electron density of states (DOS), the σ bonding interaction along the z-direction for both Pt@dv-Gr and Cu@dv-Gr was served as the main bonding interaction of *CO and the catalysts. Nonetheless, the overlap was stronger on Pt@dv-Gr than Cu@dv-Gr, leading to the stronger binding energy of *CO on Pt@dv-Gr with a negative deviation from the trend line. Moreover, a partial occupation of antibonding in *CHO binding with Cu, Ag, and Au SMA catalysts weakened the *CHO bond, while *CO had not faced this kind of antibonding, leading to the strong binding energy of *CO, i.e., a positive deviation from the trend line for these SMAs. As a consequence, the free energy difference between these two intermediates increased, leading to a larger limiting potential. On the other

hand, such an antibonding did not appear for Pt@dv-Gr, resulting in a lower free energy difference for *CO and *CHO intermediates, and consequently, a more favorable limiting potential.[130]

4.5. Methanol production on SMA catalysts

Cui et al. [129] investigated M@C_2N (M=Ti, Mn, Fe, Co, Ni, Cu, Rh, and Ru) as SMA catalysts for the ECR. They compared the *H formation with either *COOH or *OCHO formation. Accordingly, the difference in the Gibbs free energy (ΔG) of the ECR intermediates were more negative than that of the HER, suggesting the feasibility of such catalysts for the ECR and suppressing H_2 production (**Figure 19a**). Nonetheless, at the N-site opposite of the C-site of C_2N, the ΔG for the HER was negative (-0.67 eV), indicating the possibility of N-site to act as an active site for this reaction.

The binding energy of *CHO vs. *COH was also plotted, and all M@C_2N SMA catalysts showed that the protonation of *CO intermediate results in *CHO formation (**Figure 19b**). Interestingly, in the next step, all M@C_2N SMA catalysts generated *CH_2O intermediate. While, in the next hydrogenation step, Ti, Co, and Mn@C_2N SMA catalysts formed *CH_3O intermediate (**Figure 19c**) —bonded to the metal through its oxygen atom— other SMA catalysts formed *CH_2OH intermediate —bonded to the metal through its carbon atom (**Figure 19d**). The relative strength of carbophilicity and oxophilicity of the metal atom determines which intermediate should be formed, which consequently makes Ni and Fe SMA catalysts, for example, selective for methanol formation. M@C_2N catalyst with *CH_3O intermediate generated CH_4 as the final product, while others with *CH_2OH intermediate generated CH_3OH. It is worth mentioning that reaction environment conditions such as electrolyte, electric field, and pH effects are neglected in this study. Thus, the energetic picture of the reaction pathways provided here does not capture these reaction environment effects.

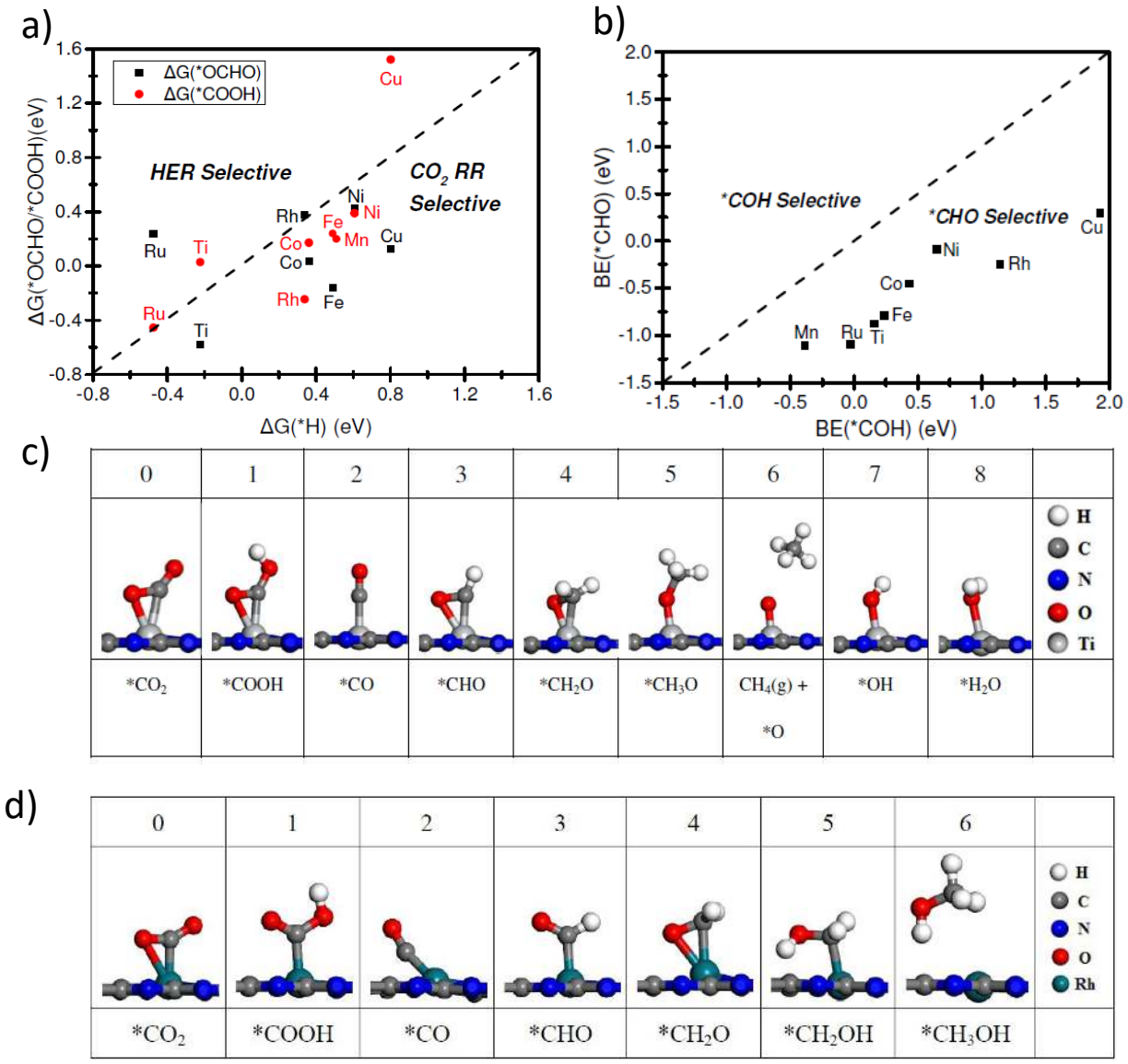

Figure 19. a) Gibbs free energy changes (ΔG) for the first protonation step of ECR vs. HER; b) Gibbs free energy changes (ΔG) for *CHO formation vs. *COH formation; c) DFT-optimized structures along the primary reaction pathway of ECR, forming CH_4 via *COOH route on Ti@C_2N; d) DFT-optimized structures along the primary reaction pathway of ECR, forming CH_3OH via *COOH route on Rh@C_2N. Reproduced with permission from reference [129]. Copyright 2018 Royal Society of Chemistry.

In another computational study, Wang et al. [135] considered 12 different transition metals as SMA catalysts on the porphyrin-like graphene support. Their computational results revealed that Co, Rh, and Ir SMA catalysts, possess a moderate *CO adsorption energy, suitable for the ECR.

Comparing the cohesive energy of Co, Rh, and Ir in their bulk metals (-3.91, -5.08, and -5.13 eV, respectively) with the adsorption energy of their single atoms embedded into porphyrin-like graphene (-8.21, -7.55, and -8.53 eV, respectively), revealed that they are strongly adsorbed on the porphyrin-like graphene support. Hence, enhancing the stability of such SMA catalysts. Among these SMA catalysts, Co showed the strongest interaction with $*CH_2O$ intermediate, a key element for methanol formation. Analyses of the electronic structure showed that the overlapping of the metal *d*-orbital with *p*-orbital of the C or O atom of $*CH_2O$ for CoN_4 is relatively stronger (with larger binding energy) in comparison to its counterparts RhN_4 and IrN_4, leading to a stronger intermediate-catalyst interaction. As a result, $*CH_2O$ intermediate could be further reduced on CoN_4 and generate CH_3OH while, owing to its relatively weaker intermediate-catalyst interaction, it desorbs as the final product from the surface of the RhN_4 and IrN_4 SMA catalysts.

4.6. Coordination atoms effect on the electronic structure of SMA catalysts

Cheng et al. [98] performed DFT computations to comprehend the effect of coordination atoms on the electronic structure of SMAs. They considered seven different saturated and unsaturated Ni-N species (**Figure 20a**). The ECR mechanism toward CO production divided into three steps: a) the adsorption step ($CO_2 \rightarrow *COOH$) followed by converting carboxyl intermediate to *CO ($*COOH \rightarrow *CO$), and finally, the desorption step ($*CO \rightarrow CO(g)$). The relation between these steps showed a correlation with the binding free energy of CO on these catalysts (**Figure 20b**). According to the Sabatier principle, the CO should bind to the catalyst's surface neither too strong nor too weak to improve the reaction rate. As seen in **Figure 20b**, the saturated Ni-N species such as $NiN_4(\text{plane})$, $NiN_4(\text{edge})$, $NiN_2(NH_2)_2$, and $NiN_3(NH_2)$ possess quite high and unfavorable reaction energy for the adsorption step. On the other hand, NiN_2 and $NiN_3(\text{plane})$ possess desirable adsorption energy, yet for the desorption step, they show poor activity. 3-coordinate edge-anchored structures, however, thanks to their desired adsorption and desorption energy, demonstrate the most active site for converting CO_2 into CO.[98]

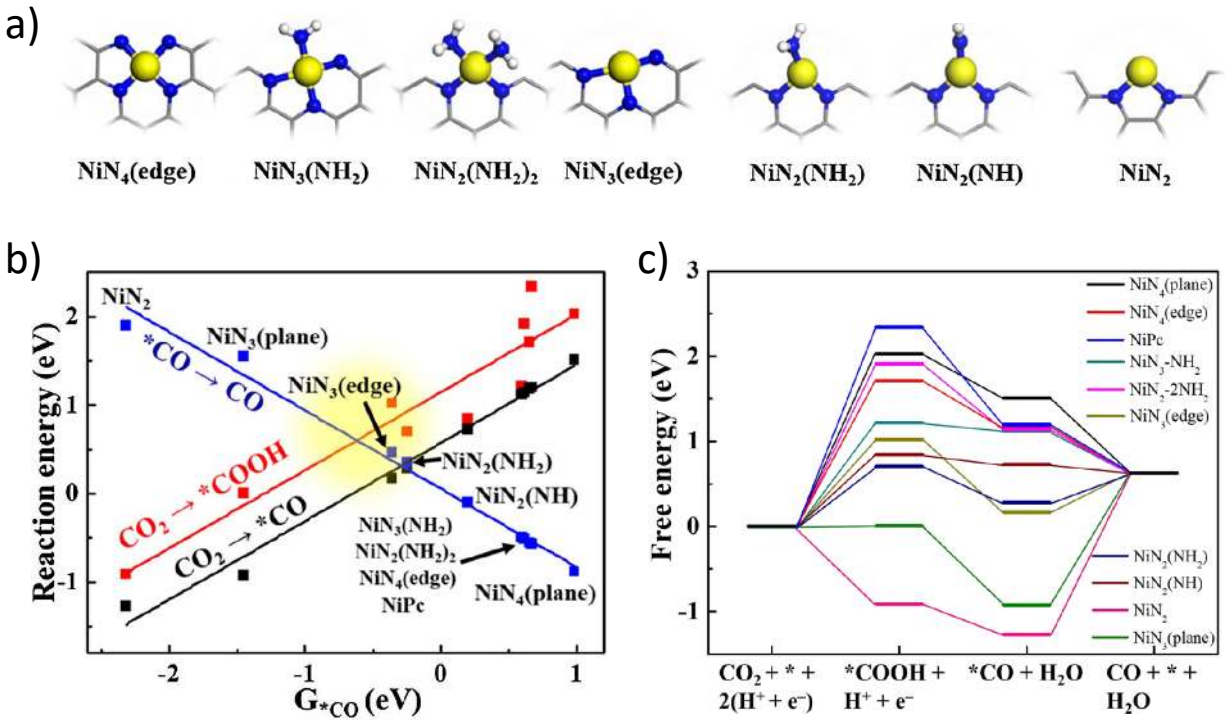

Figure 20. a) Different Ni-N active site structures on the edges of graphene sheets; b) The reaction energy is in a linear relationship with the adsorption free energy of *CO (G_{*CO}) on the active sites. Lower reaction energy indicates higher reactivity. Different Ni-N structures were located in the lines. A lower G_{*CO} indicates weaker adsorption. The region around the intersection point of the higher adsorption and desorption steps (shown in yellow) indicates the optimal reactivity; c) Reaction energy profile of different pathways. Reproduced with permission from reference [98]. Copyright 2019 Elsevier.

As shown in **Figure 20c**, *CO intermediate binds strongly to the catalyst for NiN_2 and $NiN_3(plane)$ active sites. It makes the desorption of *CO and producing of CO(g) difficult, leading to the poison of the catalyst. Conversely, the energy barriers for $NiN_4(plane)$, $NiN_4(edge)$, $NiN_2(NH_2)_2$, and $NiN_3(NH_2)$ are too high. Thus, such configurations could not serve as active sites either.[98] This study reveals the important role of the coordination atoms, their nature, and number, in altering the electronic structure of the SMA and thereby the reaction mechanism of the ECR on these catalysts. This opens a new window to further optimize the catalytic activity of SMA catalysts by altering their coordination environment, rather than merely changing the identity of the metal atom.

4.7. In situ spectroscopy

Computational DFT studies are paramount to understand the reaction mechanism; nevertheless, it is always more accurate when results are validated by the experiment. Therefore, the combined use of computational DFT and experimental methods enables the accomplishment of a deeper understanding of the reaction mechanism that cannot be achieved by the use of either approach alone. In particular, observing reaction intermediates for a proposed reaction mechanism is considered as strong evidence for that reaction pathway to exist. In recent years, several *in situ* and *operando* Raman and IR studies are reported for the ECR but mostly are performed on regular metal catalysts. [109] To the best of our knowledge, there are only a few *operando* Raman or IR spectroscopy reports on SMA catalysts for the ECR,[105-106] which calls for further studies in this area.

It is noteworthy that understanding of reaction pathways, as well as detecting of the reaction intermediates via in situ spectroscopies, even on regular electrocatalysts are still challenging. This because of the complicated nanostructured surface of the electrocatalyst and support, complicated reaction environment as a result of the electrolyte, solvated as well as adsorbed species, applied potential, and the transmutation of products—both gas or liquid ones—at the surface of the catalyst.[136] Moreover, as mentioned earlier in section 4.1, each product follows different pathways, and there exist various complex intermediates with low concentration, which make it extremely difficult to recognize them accurately. Furthermore, the reactions are faster than that it would be practical for conventional spectroscopies to identify the evolutions of the intermediates on the surface of catalysts.[137] In addition, each method has its condition requirements, and developing a system in which ECR could occur while satisfying those requirements is the major challenge.[138] For instance, X-ray photoelectron spectroscopy (XPS) is considered as a powerful tool for investigation of the composition as well as electronic structures of solid materials, however, conventional XPS work under ultra-high vacuum conditions, thus, inhibiting real-time measurements, and the analysis is confined to before and after electroreduction reaction.[139, 140] For this particular example, to overcome conventional XPS problems, a new type of XPS has been devised, which can operate at relatively higher pressures, known as near ambient pressure XPS (NAP-XPS). NAP-XPS could be used for in situ measurements.[140] Also, X-ray Absorption Spectroscopy (XAS) is another powerful tool which is able to provide beneficial information

regarding local geometric and electronic structure at ambient conditions, but the attained information is an average of bulk properties that might not be desired for SMA catalysts.[109] In situ vibrational spectroscopic methods such as Raman and IR have the potential to provide more information about the reaction intermediates; however, it is worth mentioning that due to the nature of the SMA catalysts—for having separated active sites— it would be difficult to distinguish between adsorbates bound to the SMA and other atoms.

In a gas-phase CO_2 reduction study, Wang et al. [106] studied Pt SMA and Pt cluster anchored on CeO_2 and observed quite different activity and selectivity for CO_2 conversion; while Pt as the SMA catalyst produced CO(g) as the exclusive, final product, Pt cluster produced both CO(g) and $CH_4(g)$, depending on the reaction temperature. They used *in situ* diffuse reflectance infrared Fourier transform spectroscopy (DRIFTS) to delve deep into the mechanistic difference governing the different selectivity and activity of Pt supported on CeO_2 as the single atom metal catalyst ($0.05Pt/CeO_2$) and the cluster ($2Pt/CeO_2$).

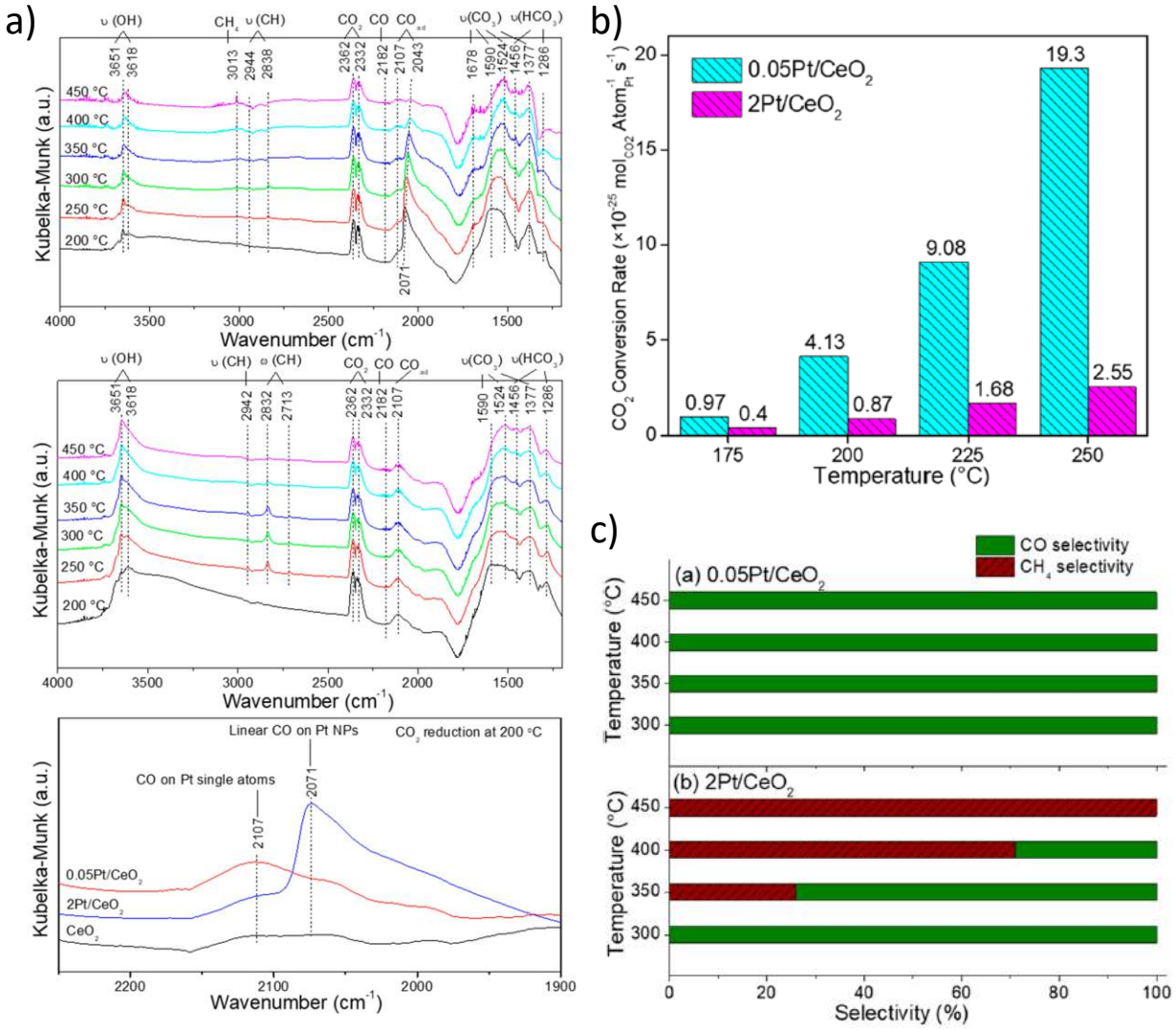

Figure 21. a) *In situ* DRIFTS spectra of $2Pt/CeO_2$ and $0.05Pt/ CeO_2$ during CO_2 reduction at temperatures ranging from 200 to 450 °C, and neat CeO_2 and the Pt/CeO_2 catalysts during CO_2 reduction at 220 °C (only the region between 2250 and 1900 cm^{-1} is shown to highlight CO adsorption); b) CO_2 conversion rate for $0.05Pt/CeO_2$ and $2Pt/CeO_2$ catalysts evaluated based on exposed Pt atoms; c) Catalytic performance selectivity of $0.05Pt/CeO_2$ and $2Pt/CeO_2$ toward CO and CH_4. Reproduced with permission from reference [106]. Copyright 2018 American Chemical Society.

The adsorbed CO is the very key intermediate, which can disclose the difference between products of $0.05Pt/CeO_2$ and $2Pt/CeO_2$. Hence, the authors explored the spectra between the 2250 and 1900 cm^{-1} wavenumber region. As seen in **Figure 21a**, both $0.05Pt/CeO_2$ and $2Pt/CeO_2$ show

a peak at 2107 cm^{-1} which is attributed to the linearly adsorbed CO on single atoms of Pt. Furthermore, another band at 2071 cm^{-1} can be seen on the 2Pt/CeO_2, which is ascribed to the linearly adsorbed CO on Pt NPs. It is noteworthy that the CeO_2 spectra indicate no peaks in this specific region, which states that the only adsorption sites for CO are Pt atoms/cluster. As shown in **Figure 21a**, the 2Pt/CeO_2 catalyst displays stronger CO_{ad} peaks than those of the 0.05Pt/CeO_2 catalyst, suggesting the weaker CO bond on the latter one, which is in good agreement with observing $CO_{(g)}$ product as the exclusive product of this catalyst. The strong binding of adsorbed CO on 2Pt/CeO_2, however, allows further protonation steps and the formation of methane. Noticeably, the adsorbed CO peak is more intense at lower temperatures for both catalysts, especially for 2Pt/CeO_2 (**Figure 21a**). For the case of 2Pt/CeO_2, such a strong bond poisons active sites, and consequently lowers CO_2 conversion, which is corresponded to the experimental results (**Figure 21b**). In addition, by increasing the temperature, the intensity of the CH_4 peak on the 2Pt/CeO_2 increases, while the adsorbed CO peak decreases dramatically, which is compatible with the observed selectivity of these products (**Figure 21c**). Therefore, it is evident that *operando* spectroscopy is a viable and powerful method to detect reaction intermediates and understand the possible reaction mechanism.

5. Electrochemical devices

Practical ECR usually requires electrochemical devices to operate at current densities higher than 200 mA cm^{-2}. To date, most of the SMA catalysts operate at a low current density range (<50 mA cm^{-2}) because they are tested in an aqueous CO_2 reduction system (H-cell), where the reaction rate is limited by the diffusion of CO_2 in aqueous media. To operate at high current densities, catalysts are often deposited on a hydrophobic gas diffusion layer, forming a gas diffusion electrode (GDE).[6, 9, 21, 23] This electrode configuration significantly reduces the diffusion path length of CO_2 to the catalyst surface, increasing CO_2 availability for a high reaction rate. In general, GDEs are integrated into two types of CO_2 electrochemical devices: flow-cell and membrane electrode assembly (MEA) electrolyzers. Here, we will briefly introduce these electrochemical devices and highlight some recent progress on SMA operated at high current densities.

5.1. Flow-cell

Flow-cell reactors comprise three main compartments for gas feedstock, liquid catholyte, and liquid anolyte. The GDE separates the gas and catholyte compartments while an ion-exchange membrane is usually used to separate the catholyte and anolyte chambers. During the reaction, CO_2 gas is flown through the gas chamber, and a flow of liquid electrolyte is pumped through the catholyte chamber located between the GDE and the membrane. The gas products are diffused back to the CO_2 gas phase while the liquid products enter the liquid electrolyte. The anolyte is pumped through the anode chamber, bringing the O_2 gas produced from the oxygen evolution reaction at the anode together with the liquid electrolyte. The presence of the catholyte in flow cells allows for fine-tuning the reaction environment to achieve high CO_2 conversion efficiency.[10-11, 21, 121] The pH and nature of the cations in the electrolyte are important parameters that influence the reaction on the cathode.

While it is still limited, SMA catalysts have been demonstrated as active and selective catalysts for CO_2 reduction to CO in a flow-cell. For example, Yang et al. incorporated Ni-single atom catalyst into the carbon fiber membrane and used it as the gas diffusion electrode for CO_2 reduction (**Figure 22a**).[141] Using an H-cell reactor, the SMA catalyst exhibited a high CO Faradaic efficiency of up to 90%, but CO partial current density was limited to less than 60 mA cm^{-2} (**Figure 22c, d**). When a flow-cell was employed, the CO partial current density increased to more than 300 mA $cm^{-2,}$ while CO Faradaic efficiencies were maintained at higher than 80%. In this work, the catalyst deposited on the carbon fiber acts as both catalysts and gas diffusion layers. Its high hydrophobicity enables the catalyst to operate at 300 mA cm^{-2} for 120 hours without any noticeable loss in selectivity (FE for CO ~ 90%) (**Figure 22b**). In another work, Gu et al. deposited the catalyst Fe^{3+}–N–C on a gas diffusion layer and the electrolysis conducted in a flow cell showed a CO partial current density of 94 mA cm^{-2} at an FE of 90%.[42] These results show that SMA can be efficiently operated at high current densities, indicating its potential for practical application.

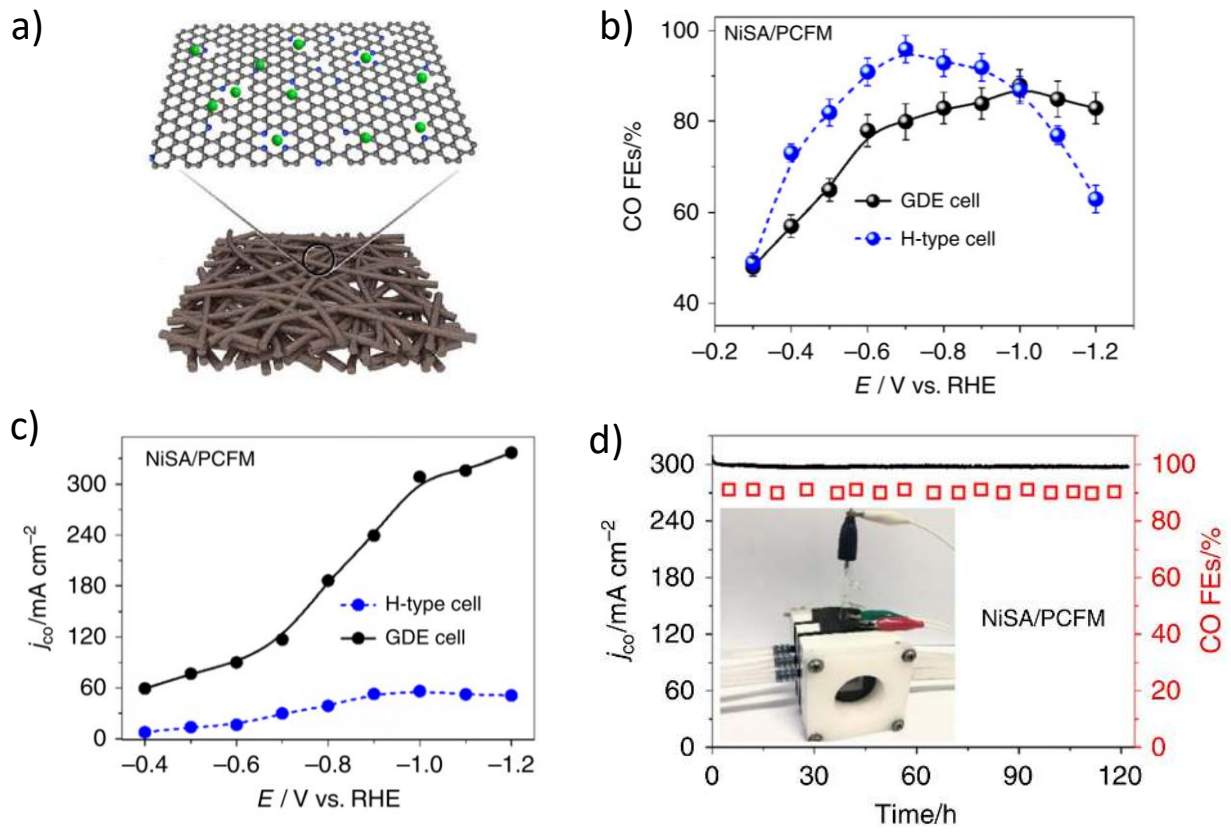

Figure 22. CO_2 electroreduction on single-atom/porous carbonfiber membrane catalyst (NiSA/PCFM) using a flow-cell reactor. a) Illustration of Ni SMA catalyst incorporated into carbon fiber electrode; b) CO faradaic efficiencies; c) Partial current densities of NiSA/PCFM at various cathode potentials in different cells; d) Long-term stability tests in flow-cell using 1 M KOH electrolyte. Reproduced with permission from reference [141]. Copyright 2020 Nature.

In ECR using flow-cells, the oxygen evolution reaction in the anode side can be operated in either alkaline or neutral media.[42, 141-142] While the operating conditions at the anode side do not affect directly the activity and selectivity of the CO_2 reduction in the cathode side, they influence the kinetics of the oxygen evolution reactions, and thus the overall efficiency of the ECR process. The kinetics of the oxygen evolution reaction is often slow in neutral media, requiring a high overpotential to achieve the desired reaction rate.[143] In addition, expensive noble metal-based catalysts such as IrO_2 are needed for efficient and stable oxygen evolution reactions in neutral media. In contrast, alkaline media are more favorable for oxygen evolution as they enable the employment of active, stable, and earth-abundant oxygen evolution catalysts with low overpotentials, such as a mixed metal oxide/hydroxide of Ni and Fe,[144] which is critical for

practical applications. However, operating the anodic reaction in alkaline media requires employing either a bipolar membrane or an alkaline catholyte.[21] The high transport resistance of the bipolar membrane leads to large ohmic losses at high current densities[145], while the degradation of the alkaline catholyte due to the carbonate formation requires an additional electrolyte regeneration process. Thus, optimizing the membranes and operating conditions for anodic reactions is needed for practical ECR.

The flow-cell reactor serves a great model for studying the performance of SMA catalysts at high current densities. The presence of the liquid catholyte is beneficial to controlling the reaction environment,[42] but it is also a source of instability in the system due to the potential penetration of liquid electrolyte into the GDE, i.e., flooding. This liquid layer also increases the overall cell resistance, leading to large total cell voltages at high current densities. This limitation can be overcome by using MEA electrolyzers.

5.2 Membrane electrode assembly cell

In MEA cells, the GDE and anode catalyst is pressed on both sides of a membrane, forming a multilayer configuration with zero-gap between cathode, membrane, and anode (**Figure 23a**). In this configuration, no liquid electrolyte is used for the cathode side, and the water reactant is provided through a vapor phase or water migration from the anode. The elimination of the catholyte reduces the cell resistance due to Ohmic loss and, at the same time, minimizes the GDE flooding issue.[22, 146] MEA cells have been used for high-rate CO_2 electroreduction to CO using SMA catalysts. For example, Jiang et al. prepared N-doped graphene atomically dispersed with Ni atoms (Ni-NG) and investigated its performance using MEA system.[66] The catalysts exhibited a current density of ~50 mA cm^{-2}, and a FE_{CO} of 97% (**Figure 23b, c**). This performance was shown to maintain for at least 8 hours of continuous electrolysis and produce 630 mL of CO gas. Zheng et al. used commercially available carbon blacks (CBs) with an activated surface to trap Ni single atoms (Ni-NCB).[62] The authors applied Ni-NCB into an anion MEA in which the humidified CO_2 gas was supplied to the cathode. A high current density of 130 mA cm^{-2} at the cell voltage of 2.7 V was achieved while the FE_{CO} remains at ~100% and the FE_{H2} was suppressed to below 1%. To demonstrate the practicability of this system for CO_2 reduction to CO, the authors customized an even larger cell, with a 10×10 cm^2 anion MEA. A current of 8.3 A (current density of 80 mA cm^{-2}) and FE_{CO} ~ 99% were recorded at the cell voltage of 2.8 V. Over 6 hours of continuous

electrolysis at the current of ~8 A, 20.4 L of CO was generated; however, the CO selectivity decreased to ~90%.

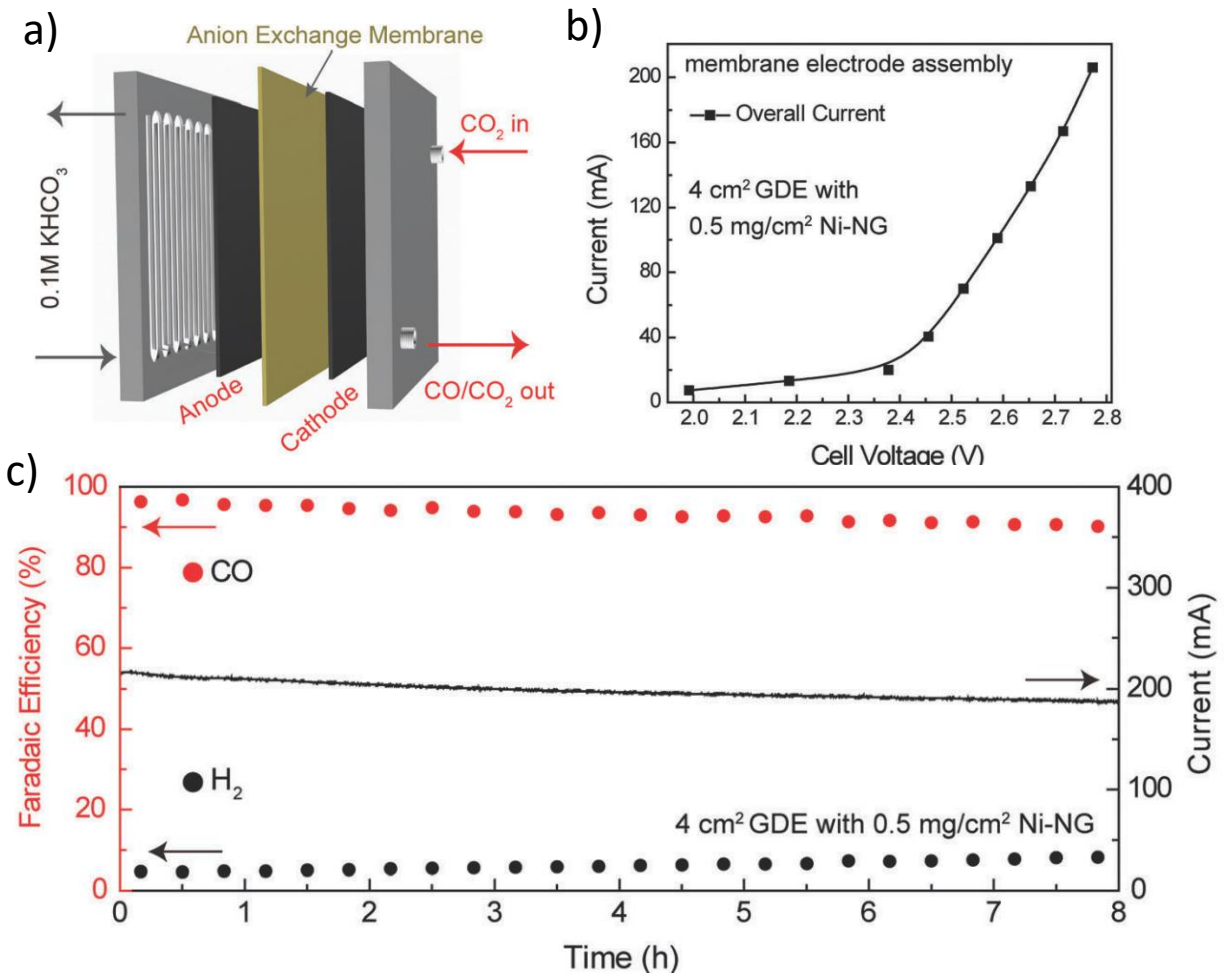

Figure 23. ECR performance on the Ni–NG catalyst by MEA cell. a) Schematic of the anion MEA, with a cathode of Ni–NG for the CO_2 reduction and an anode of IrO_2 for the oxygen evolution reaction; b) The steady-state current of Ni–NG on the 4 cm^2 electrode; c) Long-term electrolysis under a full-cell voltage of 2.78 V, showing a stable current of 200 mA (current density of ~ 50 mA cm^{-2}) and a CO selectivity of ~95%. Reproduced with permission from reference [66]. Copyright 2018 Royal Society of Chemistry.

From the application aspect, MEAs resemble the commercially existing polymer electrolyte membrane fuel-cells and electrolyzers, allowing them to be readily integrated into these matured technologies. To date, MEA cells are mainly used for CO production with SMA catalysts. For CO_2 reduction to multiple carbon products, controlling the local environment on the surface of the

catalyst is a critical factor. The lack of liquid catholyte in the MEA system makes it difficult to achieve this goal. Well-designed electrodes with the capacity of tailoring the local environment are vital for MEA electrolyzers. In this aspect, SMA catalysts with the tunable local environment of the active sites would be a potential candidate for hydrocarbon and oxygenate production using MEA systems.

6. Summary and Outlook

The SMA catalysts with single atom active sites and tunable coordination environments could take advantage of a selective homogeneous catalyst and the durability of a heterogeneous one. This unique catalytic active site structure makes them exhibit different catalytic properties compared to nanoparticle catalysts. SMA catalysts also allow for maximizing the use of the metal as an active site for the reaction. The SMA catalysts for CO_2 reduction are mainly based on inexpensive and earth-abundant elements, making them a potential candidate for practical and widespread CO_2 reduction applications.

In this review, we have discussed the relation between the structure and catalytic performance of SMA catalysts in ECR. Various SMA catalyst synthesis approaches, including one-step or multiple-steps, have been briefly described. We have also discussed important catalytic properties of SMA in CO_2 reduction, including how competing HER is suppressed, the scaling relation that makes SMA more selective for CO production, and the challenge in making multi-carbon products using SMA catalysts. Recent strategies for improving the performance of SMA catalysts, such as tuning the nature of the metal active site and its coordinating environment, have been reviewed. Finally, we have briefly discussed the potential application of SMA catalysts in CO_2 electroreduction under practical conditions.

Though significant progress in SMA catalysts development has been made, improvements in energy efficiency, selectivity, rate of reduction, and long-term stability remain on the path toward their practical applications. In addition, most SMA catalysts produce CO or formate, and their selectivity for hydrocarbons is still much lower compared to that of nanoparticle catalysts and is far from a desirable target for practical application. Developing SMA catalysts that are active and selective for multi-carbon product formation is crucial but still very challenging To achieve these goals, further advances in synthesis approaches and understanding of the CO_2 reduction mechanism on SMA are needed.

The content of metal loading significantly influences catalytic activity, as the higher the loading, the larger the number of active sites, and consequently, the higher the catalytic activity. However, in most reported works, the amount of metal loading is only around a few weight percent. In cases that we were able to achieve higher metal doping amounts, the metal sites were buried within the substrates or the binding agent, rendering them catalytically inactive. Therefore, there is still a need to explore effective methods to increase the loading of active metal atoms on the substrate. Besides, increasing the porosity of the substrates might allow for more efficient diffusion of CO_2 gas to the catalytic sites. The coordination environment around the metal atom is crucial for the stability and performance of the catalyst and needs to be systematically studied. In ECR, two or more active sites are usually required to effectively produce C_{2+} products. In this context, the development of diatomic and triatomic catalysts might lead to unique catalytic properties and might allow for the selective production of C_{2+} products.

Compared to regular metallic catalysts used for the ECR, there are only a few mechanistic studies on SMA catalysts. These studies, which are mostly based on DFT calculations, revealed the underlying mechanism for the suppression of the competing HER. While suppression of the HER is mainly due to the lack of similar active sites in close proximity, the main reason causes the lack of multi-carbon formation on SMA catalysts. On the other hand, it is observed that SMA catalysts can break the scaling rules and provide opportunities for steering the reaction path toward desired products without being limited by the scaling relations. There are few studies on transition metal SMA catalysts to provide the reaction energy diagram; however, these DFT computations are often under the most simplistic simulation conditions without considering the reaction environment. Therefore, to achieve a more realistic picture of the reaction energy diagram, it is essential to include reaction environment parameters such as water (implicit or explicit), cations, electric field, and pH in DFT computations. It is apparent that there is still a big gap in understanding the ECR mechanism on SMA catalysts compared to their counterpart regular catalysts, which might be filled by more intensive computational studies. These computations will not only shed light on the reaction mechanism but also can provide a considerable number of data for further data analysis through a machine learning approach to further guide the catalyst design.

In situ and *operando* spectroscopy are considered as another powerful technique that provides a unique mechanistic and molecular level understanding of the reaction. While powerful, it is also challenging to design the spectroscopy experiments, especially Raman and IR, so that to ensure

the attained spectra are solely from the single active sites. However, the positive side is that active sites on SMA catalysts are uniform and homogeneous, unlike regular catalysts. Therefore, once the spectra are assigned to active sites, the concerns about differences in active sites, and their possible effects on the spectra would be minimized. While it is shown that *operando* Raman or IR can significantly improve the understanding of the reaction mechanism by detecting the reaction intermediates, unfortunately, the number of these spectroscopic studies on SMA catalysts, especially for the ECR, is very limited and needs more efforts on this matter.

Finally, although many selective SMA catalysts have been reported, most of them operate at low current densities (<50 mA cm^{-2}) in aqueous systems. For practical applications, it is necessary to perform CO_2 reduction using a GDE, which allows attaining an industrially relevant current density (> 300 mA cm^{-2}). At high current densities, the local environment on the surface of the catalyst drastically changes, affecting the overall CO_2 reduction mechanism and performance. Thus, the design and optimization of the SMA catalyst should be combined with GDE and system optimization to bring this technology closer to practical applications.

Acknowledgements

T.N.N thanks Helen Co., Ltd for support. C.T.D acknowledges the financial support from the Natural Sciences and Engineering Research Council of Canada (NSERC) and Queen's University.

Notes

The authors declare no competing financial interest.

References

1. Chu, S.; Majumdar, A., Opportunities and Challenges for a Sustainable Energy Future. *Nature* **2012,** *488*, 294-303.

2. Annual Energy Outlook 2019. https://www.eia.gov/outlooks/aeo/pdf/aeo2019.pdf (accessed August 05, 2020).

3. Chu, S.; Cui, Y.; Liu, N., The Path towards Sustainable Energy. *Nat. Mater.* **2016,** *16*, 16.

4. Yan, Z.; Hitt, J. L.; Turner, J. A.; Mallouk, T. E., Renewable Electricity Storage Using Electrolysis. *Proc. Natl. Acad. Sci. USA* **2020,** *117*, 12558.

5. De Luna, P.; Hahn, C.; Higgins, D.; Jaffer, S. A.; Jaramillo, T. F.; Sargent, E. H., What Would It Take for Renewably Powered Electrosynthesis to Displace Petrochemical Processes? *Science* **2019,** *364*, eaav3506.

6. Ross, M. B.; De Luna, P.; Li, Y.; Dinh, C.-T.; Kim, D.; Yang, P.; Sargent, E. H., Designing Materials for Electrochemical Carbon Dioxide Recycling. *Nat. Catal.* **2019**, *2*, 648-658.

7. Nitopi, S.; Bertheussen, E.; Scott, S. B.; Liu, X.; Engstfeld, A. K.; Horch, S.; Seger, B.; Stephens, I. E. L.; Chan, K.; Hahn, C.; Nørskov, J. K.; Jaramillo, T. F.; Chorkendorff, I., Progress and Perspectives of Electrochemical CO_2 Reduction on Copper in Aqueous Electrolyte. *Chem. Rev.* **2019,** *119*, 7610-7672.

8. Seh, Z. W.; Kibsgaard, J.; Dickens, C. F.; Chorkendorff, I.; Nørskov, J. K.; Jaramillo, T. F., Combining Theory and Experiment in Electrocatalysis: Insights into Materials Design. *Science* **2017,** *355*, eaad4998.

9. Kibria, M. G.; Edwards, J. P.; Gabardo, C. M.; Dinh, C.-T.; Seifitokaldani, A.; Sinton, D.; Sargent, E. H., Electrochemical CO_2 Reduction into Chemical Feedstocks: From Mechanistic Electrocatalysis Models to System Design. *Adv. Mater.* **2019,** *31*, 1807166.

10. Gabardo, C. M.; Seifitokaldani, A.; Edwards, J. P.; Dinh, C.-T.; Burdyny, T.; Kibria, M. G.; O'Brien, C.; Sargent, E. H.; Sinton, D., Combined High Alkalinity and Pressurization Enable Efficient CO_2 Electroreduction to CO. *Energy Environ. Sci.* **2018,** *11*, 2531-2539.

11. Dinh, C.-T.; García de Arquer, F. P.; Sinton, D.; Sargent, E. H., High Rate, Selective, and Stable Electroreduction of CO_2 to CO in Basic and Neutral Media. *ACS Energy Lett.* **2018,** *3*, 2835-2840.

12. Verma, S.; Hamasaki, Y.; Kim, C.; Huang, W.; Lu, S.; Jhong, H.-R. M.; Gewirth, A. A.; Fujigaya, T.; Nakashima, N.; Kenis, P. J. A., Insights into the Low Overpotential Electroreduction of CO_2 to CO on a Supported Gold Catalyst in an Alkaline Flow Electrolyzer. *ACS Energy Lett.* **2018,** *3*, 193-198.

13. Lu, Q.; Rosen, J.; Zhou, Y.; Hutchings, G. S.; Kimmel, Y. C.; Chen, J. G.; Jiao, F., A Selective and Efficient Electrocatalyst for Carbon Dioxide Reduction. *Nat. Commun.* **2014,** *5*, 3242.

14. Chen, Y.; Li, C. W.; Kanan, M. W., Aqueous CO_2 Reduction at Very Low Overpotential on Oxide-Derived Au Nanoparticles. *J. Am. Chem. Soc.* **2012,** *134*, 19969-19972.

15. Liu, M.; Pang, Y.; Zhang, B.; De Luna, P.; Voznyy, O.; Xu, J.; Zheng, X.; Dinh, C. T.; Fan, F.; Cao, C.; de Arquer, F. P. G.; Safaei, T. S.; Mepham, A.; Klinkova, A.; Kumacheva, E.; Filleter, T.; Sinton, D.; Kelley, S. O.; Sargent, E. H., Enhanced Electrocatalytic CO_2 Reduction via Field-Induced Reagent Concentration. *Nature* **2016,** *537*, 382-386.

16. Fan, M.; Prabhudev, S.; Garbarino, S.; Qiao, J.; Botton, G. A.; Harrington, D. A.; Tavares, A. C.; Guay, D., Uncovering the Nature of Electroactive Sites in Nano Architectured Dendritic Bi for Highly Efficient CO_2 Electroreduction to Formate. *Appl. Catal. B: Environ.* **2020,** *274*, 119031.

17. Fan, M.; Garbarino, S.; Botton, G. A.; Tavares, A. C.; Guay, D., Selective Electroreduction of CO_2 to Formate on 3D [100] Pb Dendrites with Nanometer-Sized Needle-Like Tips. *J. Mater. Chem. A* **2017,** *5*, 20747-20756.

18. Klinkova, A.; De Luna, P.; Dinh, C.-T.; Voznyy, O.; Larin, E. M.; Kumacheva, E.; Sargent, E. H., Rational Design of Efficient Palladium Catalysts for Electroreduction of Carbon Dioxide to Formate. *ACS Catal.* **2016,** *6*, 8115-8120.

19. Liu, M.; Liu, M.; Wang, X.; Kozlov, S. M.; Cao, Z.; De Luna, P.; Li, H.; Qiu, X.; Liu, K.; Hu, J.; Jia, C.; Wang, P.; Zhou, H.; He, J.; Zhong, M.; Lan, X.; Zhou, Y.; Wang, Z.; Li, J.; Seifitokaldani, A.; Dinh, C. T.; Liang, H.; Zou, C.; Zhang, D.; Yang, Y.; Chan, T.-S.; Han, Y.; Cavallo, L.; Sham, T.-K.; Hwang, B.-J.; Sargent, E. H., Quantum-Dot-Derived Catalysts for CO_2 Reduction Reaction. *Joule* **2019,** *3*, 1703-1718.

20. Luc, W.; Ko, B. H.; Kattel, S.; Li, S.; Su, D.; Chen, J. G.; Jiao, F., SO_2-Induced Selectivity Change in CO_2 Electroreduction. *J. Am. Chem. Soc.* **2019,** *141*, 9902-9909.

21. Dinh, C.-T.; Burdyny, T.; Kibria, M. G.; Seifitokaldani, A.; Gabardo, C. M.; García de Arquer, F. P.; Kiani, A.; Edwards, J. P.; De Luna, P.; Bushuyev, O. S.; Zou, C.; Quintero-Bermudez, R.; Pang, Y.; Sinton, D.; Sargent, E. H., CO_2 Electroreduction to Ethylene via Hydroxide-Mediated Copper Catalysis at an Abrupt Interface. *Science* **2018,** *360*, 783-787.

22. Li, F.; Thevenon, A.; Rosas-Hernández, A.; Wang, Z.; Li, Y.; Gabardo, C. M.; Ozden, A.; Dinh, C. T.; Li, J.; Wang, Y.; Edwards, J. P.; Xu, Y.; McCallum, C.; Tao, L.; Liang, Z.-Q.; Luo, M.; Wang, X.; Li, H.; O'Brien, C. P.; Tan, C.-S.; Nam, D.-H.; Quintero-Bermudez, R.; Zhuang, T.-T.; Li, Y. C.; Han, Z.; Britt, R. D.; Sinton, D.; Agapie, T.; Peters, J. C.; Sargent, E. H., Molecular Tuning of CO_2-to-Ethylene Conversion. *Nature* **2020,** *577*, 509-513.

23. García de Arquer, F. P.; Dinh, C.-T.; Ozden, A.; Wicks, J.; McCallum, C.; Kirmani, A. R.; Nam, D.-H.; Gabardo, C.; Seifitokaldani, A.; Wang, X.; Li, Y. C.; Li, F.; Edwards, J.; Richter, L. J.; Thorpe, S. J.; Sinton, D.; Sargent, E. H., CO_2 Electrolysis to Multicarbon Products at Activities Greater than 1 A cm^{-2}. *Science* **2020,** *367*, 661-666.

24. Lv, J.-J.; Jouny, M.; Luc, W.; Zhu, W.; Zhu, J.-J.; Jiao, F., A Highly Porous Copper Electrocatalyst for Carbon Dioxide Reduction. *Adv. Mater.* **2018,** *30*, 1803111.

25. Jiang, K.; Sandberg, R. B.; Akey, A. J.; Liu, X.; Bell, D. C.; Nørskov, J. K.; Chan, K.; Wang, H., Metal Ion Cycling of Cu Foil for Selective C–C Coupling in Electrochemical CO_2 Reduction. *Nat. Catal.* **2018,** *1*, 111-119.

26. Kibria, M. G.; Dinh, C.-T.; Seifitokaldani, A.; De Luna, P.; Burdyny, T.; Quintero-Bermudez, R.; Ross, M. B.; Bushuyev, O. S.; García de Arquer, F. P.; Yang, P.; Sinton, D.; Sargent, E. H., A Surface Reconstruction Route to High Productivity and Selectivity in CO_2 Electroreduction toward C_{2+} Hydrocarbons. *Adv. Mater.* **2018,** *30*, 1804867.

27. Liang, Z.-Q.; Zhuang, T.-T.; Seifitokaldani, A.; Li, J.; Huang, C.-W.; Tan, C.-S.; Li, Y.; De Luna, P.; Dinh, C. T.; Hu, Y.; Xiao, Q.; Hsieh, P.-L.; Wang, Y.; Li, F.; Quintero-Bermudez, R.; Zhou, Y.; Chen, P.; Pang, Y.; Lo, S.-C.; Chen, L.-J.; Tan, H.; Xu, Z.; Zhao, S.; Sinton, D.; Sargent, E. H., Copper-on-Nitride Enhances the Stable Electrosynthesis of Multi-Carbon Products from CO_2. *Nat. Commun.* **2018,** *9*, 3828.

28. Wang, L.; Nitopi, S. A.; Bertheussen, E.; Orazov, M.; Morales-Guio, C. G.; Liu, X.; Higgins, D. C.; Chan, K.; Nørskov, J. K.; Hahn, C.; Jaramillo, T. F., Electrochemical Carbon Monoxide Reduction on Polycrystalline Copper: Effects of Potential, Pressure, and pH on Selectivity toward Multicarbon and Oxygenated Products. *ACS Catal.* **2018,** *8*, 7445-7454.

29. Liu, X.; Schlexer, P.; Xiao, J.; Ji, Y.; Wang, L.; Sandberg, R. B.; Tang, M.; Brown, K. S.; Peng, H.; Ringe, S.; Hahn, C.; Jaramillo, T. F.; Nørskov, J. K.; Chan, K., pH Effects on the Electrochemical Reduction of CO_2 towards C_2 Products on Stepped Copper. *Nat. Commun.* **2019,** *10*, 32.

30. Mariano, R. G.; McKelvey, K.; White, H. S.; Kanan, M. W., Selective Increase in CO_2 Electroreduction Activity at Grain-Boundary Surface Terminations. *Science* **2017,** *358*, 1187-1192.

31. Wang, X.; Wang, Z.; Zhuang, T.-T.; Dinh, C.-T.; Li, J.; Nam, D.-H.; Li, F.; Huang, C.-W.; Tan, C.-S.; Chen, Z.; Chi, M.; Gabardo, C. M.; Seifitokaldani, A.; Todorović, P.; Proppe, A.;

Pang, Y.; Kirmani, A. R.; Wang, Y.; Ip, A. H.; Richter, L. J.; Scheffel, B.; Xu, A.; Lo, S.-C.; Kelley, S. O.; Sinton, D.; Sargent, E. H., Efficient Upgrading of CO to C_3 Fuel Using Asymmetric C-C Coupling Active Sites. *Nat. Commun.* **2019,** *10*, 5186.

32. Li, Y. C.; Wang, Z.; Yuan, T.; Nam, D.-H.; Luo, M.; Wicks, J.; Chen, B.; Li, J.; Li, F.; de Arquer, F. P. G.; Wang, Y.; Dinh, C.-T.; Voznyy, O.; Sinton, D.; Sargent, E. H., Binding Site Diversity Promotes CO_2 Electroreduction to Ethanol. *J. Am. Chem. Soc.* **2019,** *141*, 8584-8591.

33. Hoang, T. T. H.; Verma, S.; Ma, S.; Fister, T. T.; Timoshenko, J.; Frenkel, A. I.; Kenis, P. J. A.; Gewirth, A. A., Nanoporous Copper–Silver Alloys by Additive-Controlled Electrodeposition for the Selective Electroreduction of CO_2 to Ethylene and Ethanol. *J. Am. Chem. Soc.* **2018,** *140*, 5791-5797.

34. Luc, W.; Fu, X.; Shi, J.; Lv, J.-J.; Jouny, M.; Ko, B. H.; Xu, Y.; Tu, Q.; Hu, X.; Wu, J.; Yue, Q.; Liu, Y.; Jiao, F.; Kang, Y., Two-Dimensional Copper Nanosheets for Electrochemical Reduction of Carbon Monoxide to Acetate. *Nat. Catal.* **2019,** *2*, 423-430.

35. Lu, X.-L.; Rong, X.; Zhang, C.; Lu, T.-B., Carbon-Based Single-Atom Catalysts for CO_2 Electroreduction: Progress and Optimization Strategies. *J. Mater. Chem. A* **2020,** *8*, 10695-10708.

36. Lü, F.; Bao, H.; Mi, Y.; Liu, Y.; Sun, J.; Peng, X.; Qiu, Y.; Zhuo, L.; Liu, X.; Luo, J., Electrochemical CO_2 Reduction: from Nanoclusters to Single Atom Catalysts. *Sustain. Energy Fuels* **2020,** *4*, 1012-1028.

37. Su, X.; Yang, X. F.; Huang, Y.; Liu, B.; Zhang, T., Single-Atom Catalysis toward Efficient CO_2 Conversion to CO and Formate Products. *Acc. Chem. Res.* **2019,** *52*, 656-664.

38. Cheng, Y.; Yang, S.; Jiang, S. P.; Wang, S., Supported Single Atoms as New Class of Catalysts for Electrochemical Reduction of Carbon Dioxide. *Small Methods* **2019,** *3*, 1800440.

39. Li, X.; Bi, W.; Chen, M.; Sun, Y.; Ju, H.; Yan, W.; Zhu, J.; Wu, X.; Chu, W.; Wu, C.; Xie, Y., Exclusive Ni–N_4 Sites Realize Near-Unity CO Selectivity for Electrochemical CO_2 Reduction. *J. Am. Chem. Soc.* **2017,** *139*, 14889-14892.

40. Zhang, C.; Yang, S.; Wu, J.; Liu, M.; Yazdi, S.; Ren, M.; Sha, J.; Zhong, J.; Nie, K.; Jalilov, A. S.; Li, Z.; Li, H.; Yakobson, B. I.; Wu, Q.; Ringe, E.; Xu, H.; Ajayan, P. M.; Tour, J. M., Electrochemical CO_2 Reduction with Atomic Iron-Dispersed on Nitrogen-Doped Graphene. *Adv. Energy Mater.* **2018,** *8*, 1703487.

41. Cui, X.; Li, W.; Ryabchuk, P.; Junge, K.; Beller, M., Bridging Homogeneous and Heterogeneous Catalysis by Heterogeneous Single-Metal-Site Catalysts. *Nat. Catal.* **2018,** *1*, 385-397.

42. Gu, J.; Hsu, C.-S.; Bai, L.; Chen, H. M.; Hu, X., Atomically Dispersed Fe^{3+} Sites Catalyze Efficient CO_2 Electroreduction to CO. *Science* **2019,** *364*, 1091-1094.

43. Zhang, B.; Zhang, J.; Shi, J.; Tan, D.; Liu, L.; Zhang, F.; Lu, C.; Su, Z.; Tan, X.; Cheng, X.; Han, B.; Zheng, L.; Zhang, J., Manganese Acting as a High-Performance Heterogeneous Electrocatalyst in Carbon Dioxide Reduction. *Nat. Commun.* **2019,** *10*, 2980.

44. Ren, Y.; Tang, Y.; Zhang, L.; Liu, X.; Li, L.; Miao, S.; Sheng Su, D.; Wang, A.; Li, J.; Zhang, T., Unraveling the Coordination Structure-Performance Relationship in Pt_1/Fe_2O_3 Single-Atom Catalyst. *Nat. Commun.* **2019,** *10*, 4500.

45. Wang, X.; Chen, Z.; Zhao, X.; Yao, T.; Chen, W.; You, R.; Zhao, C.; Wu, G.; Wang, J.; Huang, W.; Yang, J.; Hong, X.; Wei, S.; Wu, Y.; Li, Y., Regulation of Coordination Number over Single Co Sites: Triggering the Efficient Electroreduction of CO_2. *Angew. Chem. Int. Ed.* **2018,** *57*, 1944-1948.

46. Zhou, Y.; Gao, G.; Li, Y.; Chu, W.; Wang, L.-W., Transition-Metal Single Atoms in Nitrogen-Doped Graphenes as Efficient Active Centers for Water Splitting: A Theoretical Study. *Phys. Chem. Chem. Phys.* **2019,** *21*, 3024-3032.

47. Zhao, L.; He, R.; Rim, K. T.; Schiros, T.; Kim, K. S.; Zhou, H.; Gutiérrez, C.; Chockalingam, S. P.; Arguello, C. J.; Pálová, L.; Nordlund, D.; Hybertsen, M. S.; Reichman, D. R.; Heinz, T. F.; Kim, P.; Pinczuk, A.; Flynn, G. W.; Pasupathy, A. N., Visualizing Individual Nitrogen Dopants in Monolayer Graphene. *Science* **2011,** *333*, 999-1003.

48. Luo, Z.; Lim, S.; Tian, Z.; Shang, J.; Lai, L.; MacDonald, B.; Fu, C.; Shen, Z.; Yu, T.; Lin, J., Pyridinic N Doped Graphene: Synthesis, Electronic Structure, and Electrocatalytic Property. *J. Mater. Chem.* **2011,** *21*, 8038-8044.

49. Wang, Z.; Chen, Y.; Li, P.; Zhou, J.; He, J.; Zhang, W.; Guo, Z.; Li, Y.; Dong, M., Modulation of N-Bonding Configurations and Their Influence on the Electrical Properties of Nitrogen-Doped Graphene. *RSC Adv.* **2016,** *6*, 92682-92687.

50. Yazici, M. S.; Azder, M. A.; Salihoglu, O., CVD Grown Graphene as Catalyst for Acid Electrolytes. *Int. J. Hydrogen Energy* **2018,** *43*, 10710-10716.

51. Telychko, M.; Mutombo, P.; Ondráček, M.; Hapala, P.; Bocquet, F. C.; Kolorenč, J.; Vondráček, M.; Jelínek, P.; Švec, M., Achieving High-Quality Single-Atom Nitrogen Doping of Graphene/SiC(0001) by Ion Implantation and Subsequent Thermal Stabilization. *ACS Nano* **2014,** *8*, 7318-7324.

52. Iyer, G. R. S.; Wang, J.; Wells, G.; Bradley, M. P.; Borondics, F., Nanoscale Imaging of Freestanding Nitrogen Doped Single Layer Graphene. *Nanoscale* **2015,** *7*, 2289-2294.

53. Bakandritsos, A.; Pykal, M.; Błoński, P.; Jakubec, P.; Chronopoulos, D. D.; Poláková, K.; Georgakilas, V.; Čépe, K.; Tomanec, O.; Ranc, V.; Bourlinos, A. B.; Zbořil, R.; Otyepka, M., Cyanographene and Graphene Acid: Emerging Derivatives Enabling High-Yield and Selective Functionalization of Graphene. *ACS Nano* **2017,** *11*, 2982-2991.

54. Stambula, S.; Gauquelin, N.; Bugnet, M.; Gorantla, S.; Turner, S.; Sun, S.; Liu, J.; Zhang, G.; Sun, X.; Botton, G. A., Chemical Structure of Nitrogen-Doped Graphene with Single Platinum Atoms and Atomic Clusters as a Platform for the PEMFC Electrode. *J. Phys. Chem. C* **2014,** *118*, 3890-3900.

55. Cheng, N.; Stambula, S.; Wang, D.; Banis, M. N.; Liu, J.; Riese, A.; Xiao, B.; Li, R.; Sham, T.-K.; Liu, L.-M.; Botton, G. A.; Sun, X., Platinum Single-Atom and Cluster Catalysis of the Hydrogen Evolution Reaction. *Nat. Commun.* **2016,** *7*, 13638.

56. Li, T.; Liu, J.; Song, Y.; Wang, F., Photochemical Solid-Phase Synthesis of Platinum Single Atoms on Nitrogen-Doped Carbon with High Loading as Bifunctional Catalysts for Hydrogen Evolution and Oxygen Reduction Reactions. *ACS Catal.* **2018,** *8*, 8450-8458.

57. Cui, X.; Xiao, J.; Wu, Y.; Du, P.; Si, R.; Yang, H.; Tian, H.; Li, J.; Zhang, W.-H.; Deng, D.; Bao, X., A Graphene Composite Material with Single Cobalt Active Sites: A Highly Efficient Counter Electrode for Dye-Sensitized Solar Cells. *Angew. Chem. Int. Ed.* **2016,** *55*, 6708-6712.

58. Huang, K.; Zhang, L.; Xu, T.; Wei, H.; Zhang, R.; Zhang, X.; Ge, B.; Lei, M.; Ma, J.-Y.; Liu, L.-M.; Wu, H., −60 °C Solution Synthesis of Atomically Dispersed Cobalt Electrocatalyst with Superior Performance. *Nat. Commun.* **2019,** *10*, 606.

59. Bi, W.; Li, X.; You, R.; Chen, M.; Yuan, R.; Huang, W.; Wu, X.; Chu, W.; Wu, C.; Xie, Y., Surface Immobilization of Transition Metal Ions on Nitrogen-Doped Graphene Realizing High-Efficient and Selective CO_2 Reduction. *Adv. Mater.* **2018,** *30*, 1706617.

60. Lai, Q.; Zhao, Y.; Zhu, J.; Liang, Y.; He, J.; Chen, J., Directly Anchoring Highly Dispersed Copper Sites on Nitrogen-Doped Carbon for Enhanced Oxygen Reduction Electrocatalysis. *ChemElectroChem* **2018,** *5*, 1822-1826.

61. Bakandritsos, A.; Kadam, R. G.; Kumar, P.; Zoppellaro, G.; Medved, M.; Tuček, J.; Montini, T.; Tomanec, O.; Andrýsková, P.; Drahoš, B.; Varma, R. S.; Otyepka, M.; Gawande, M. B.; Fornasiero, P.; Zbořil, R., Mixed-Valence Single-Atom Catalyst Derived from Functionalized Graphene. *Adv. Mater.* **2019,** *31*, 1900323.

62. Zheng, T.; Jiang, K.; Ta, N.; Hu, Y.; Zeng, J.; Liu, J.; Wang, H., Large-Scale and Highly Selective CO_2 Electrocatalytic Reduction on Nickel Single-Atom Catalyst. *Joule* **2019,** *3*, 265-278.

63. Zhao, L.; Zhang, Y.; Huang, L.-B.; Liu, X.-Z.; Zhang, Q.-H.; He, C.; Wu, Z.-Y.; Zhang, L.-J.; Wu, J.; Yang, W.; Gu, L.; Hu, J.-S.; Wan, L.-J., Cascade Anchoring Strategy for General Mass Production of High-Loading Single-Atomic Metal-Nitrogen Catalysts. *Nat. Commun.* **2019,** *10*, 1278.

64. Fei, H.; Dong, J.; Arellano-Jiménez, M. J.; Ye, G.; Dong Kim, N.; Samuel, E. L. G.; Peng, Z.; Zhu, Z.; Qin, F.; Bao, J.; Yacaman, M. J.; Ajayan, P. M.; Chen, D.; Tour, J. M., Atomic Cobalt on Nitrogen-Doped Graphene for Hydrogen Generation. *Nat. Commun.* **2015,** *6*, 8668.

65. Zhang, C.; Sha, J.; Fei, H.; Liu, M.; Yazdi, S.; Zhang, J.; Zhong, Q.; Zou, X.; Zhao, N.; Yu, H.; Jiang, Z.; Ringe, E.; Yakobson, B. I.; Dong, J.; Chen, D.; Tour, J. M., Single-Atomic Ruthenium Catalytic Sites on Nitrogen-Doped Graphene for Oxygen Reduction Reaction in Acidic Medium. *ACS Nano* **2017,** *11*, 6930-6941.

66. Jiang, K.; Siahrostami, S.; Zheng, T.; Hu, Y.; Hwang, S.; Stavitski, E.; Peng, Y.; Dynes, J.; Gangisetty, M.; Su, D.; Attenkofer, K.; Wang, H., Isolated Ni Single Atoms in Graphene Nanosheets for High-Performance CO_2 Reduction. *Energy Environ. Sci.* **2018,** *11*, 893-903.

67. Guan, J.; Duan, Z.; Zhang, F.; Kelly, S. D.; Si, R.; Dupuis, M.; Huang, Q.; Chen, J. Q.; Tang, C.; Li, C., Water Oxidation on a Mononuclear Manganese Heterogeneous Catalyst. *Nat. Catal.* **2018,** *1*, 870-877.

68. Fei, H.; Dong, J.; Feng, Y.; Allen, C. S.; Wan, C.; Volosskiy, B.; Li, M.; Zhao, Z.; Wang, Y.; Sun, H.; An, P.; Chen, W.; Guo, Z.; Lee, C.; Chen, D.; Shakir, I.; Liu, M.; Hu, T.; Li, Y.; Kirkland, A. I.; Duan, X.; Huang, Y., General Synthesis and Definitive Structural Identification

of MN_4C_4 Single-Atom Catalysts with Tunable Electrocatalytic Activities. *Nat. Catal.* **2018,** *1*, 63-72.

69. Fei, H.; Dong, J.; Wan, C.; Zhao, Z.; Xu, X.; Lin, Z.; Wang, Y.; Liu, H.; Zang, K.; Luo, J.; Zhao, S.; Hu, W.; Yan, W.; Shakir, I.; Huang, Y.; Duan, X., Microwave-Assisted Rapid Synthesis of Graphene-Supported Single Atomic Metals. *Adv. Mater.* **2018,** *30*, 1802146.

70. Zhou, H.-C.; Long, J. R.; Yaghi, O. M., Introduction to Metal–Organic Frameworks. *Chem. Rev.* **2012,** *112*, 673-674.

71. Liu, B.; Shioyama, H.; Akita, T.; Xu, Q., Metal-Organic Framework as a Template for Porous Carbon Synthesis. *J. Am. Chem. Soc.* **2008,** *130*, 5390-5391.

72. Jiang, H.-L.; Liu, B.; Lan, Y.-Q.; Kuratani, K.; Akita, T.; Shioyama, H.; Zong, F.; Xu, Q., From Metal–Organic Framework to Nanoporous Carbon: Toward a Very High Surface Area and Hydrogen Uptake. *J. Am. Chem. Soc.* **2011,** *133*, 11854-11857.

73. Zitolo, A.; Goellner, V.; Armel, V.; Sougrati, M.-T.; Mineva, T.; Stievano, L.; Fonda, E.; Jaouen, F., Identification of Catalytic Sites for Oxygen Reduction in Iron- and Nitrogen-Doped Graphene Materials. *Nat. Mater.* **2015,** *14*, 937.

74. Jiao, L.; Wan, G.; Zhang, R.; Zhou, H.; Yu, S.-H.; Jiang, H.-L., From Metal–Organic Frameworks to Single-Atom Fe Implanted N-doped Porous Carbons: Efficient Oxygen Reduction in Both Alkaline and Acidic Media. *Angew. Chem. Int. Ed.* **2018,** *57*, 8525-8529.

75. Chen, Y.; Ji, S.; Wang, Y.; Dong, J.; Chen, W.; Li, Z.; Shen, R.; Zheng, L.; Zhuang, Z.; Wang, D.; Li, Y., Isolated Single Iron Atoms Anchored on N-Doped Porous Carbon as an Efficient Electrocatalyst for the Oxygen Reduction Reaction. *Angew. Chem. Int. Ed.* **2017,** *56*, 6937-6941.

76. Zhao, C.; Dai, X.; Yao, T.; Chen, W.; Wang, X.; Wang, J.; Yang, J.; Wei, S.; Wu, Y.; Li, Y., Ionic Exchange of Metal–Organic Frameworks to Access Single Nickel Sites for Efficient Electroreduction of CO_2. *J. Am. Chem. Soc.* **2017,** *139*, 8078-8081.

77. Yin, P.; Yao, T.; Wu, Y.; Zheng, L.; Lin, Y.; Liu, W.; Ju, H.; Zhu, J.; Hong, X.; Deng, Z.; Zhou, G.; Wei, S.; Li, Y., Single Cobalt Atoms with Precise N-Coordination as Superior Oxygen Reduction Reaction Catalysts. *Angew. Chem. Int. Ed.* **2016,** *55*, 10800-10805.

78. Fan, L.; Liu, P. F.; Yan, X.; Gu, L.; Yang, Z. Z.; Yang, H. G.; Qiu, S.; Yao, X., Atomically Isolated Nickel Species Anchored on Graphitized Carbon for Efficient Hydrogen Evolution Electrocatalysis. *Nat. Commun.* **2016,** *7*, 10667.

79. Wei, S.; Li, A.; Liu, J.-C.; Li, Z.; Chen, W.; Gong, Y.; Zhang, Q.; Cheong, W.-C.; Wang, Y.; Zheng, L.; Xiao, H.; Chen, C.; Wang, D.; Peng, Q.; Gu, L.; Han, X.; Li, J.; Li, Y., Direct Observation of Noble Metal Nanoparticles Transforming to Thermally Stable Single Atoms. *Nat. Nanotechnol.* **2018,** *13*, 856-861.

80. Zhu, Y.; Sun, W.; Luo, J.; Chen, W.; Cao, T.; Zheng, L.; Dong, J.; Zhang, J.; Zhang, M.; Han, Y.; Chen, C.; Peng, Q.; Wang, D.; Li, Y., A Cocoon Silk Chemistry Strategy to Ultrathin N-Doped Carbon Nanosheet with Metal Single-Site Catalysts. *Nat. Commun.* **2018,** *9*, 3861.

81. Zhou, S.; Shang, L.; Zhao, Y.; Shi, R.; Waterhouse, G. I. N.; Huang, Y.-C.; Zheng, L.; Zhang, T., Pd Single-Atom Catalysts on Nitrogen-Doped Graphene for the Highly Selective Photothermal Hydrogenation of Acetylene to Ethylene. *Adv. Mater.* **2019,** *31*, 1900509.

82. Zhu, Y.; Cao, T.; Cao, C.; Luo, J.; Chen, W.; Zheng, L.; Dong, J.; Zhang, J.; Han, Y.; Li, Z.; Chen, C.; Peng, Q.; Wang, D.; Li, Y., One-Pot Pyrolysis to N-Doped Graphene with High-Density Pt Single Atomic Sites as Heterogeneous Catalyst for Alkene Hydrosilylation. *ACS Catal.* **2018,** *8*, 10004-10011.

83. Cheng, Y.; He, S.; Lu, S.; Veder, J.-P.; Johannessen, B.; Thomsen, L.; Saunders, M.; Becker, T.; De Marco, R.; Li, Q.; Yang, S.-z.; Jiang, S. P., Iron Single Atoms on Graphene as Nonprecious Metal Catalysts for High-Temperature Polymer Electrolyte Membrane Fuel Cells. *Adv. Sci.* **2019,** *6*, 1802066.

84. Cheng, Y.; Zhao, S.; Johannessen, B.; Veder, J.-P.; Saunders, M.; Rowles, M. R.; Cheng, M.; Liu, C.; Chisholm, M. F.; De Marco, R.; Cheng, H.-M.; Yang, S.-Z.; Jiang, S. P., Atomically Dispersed Transition Metals on Carbon Nanotubes with Ultrahigh Loading for Selective Electrochemical Carbon Dioxide Reduction. *Adv. Mater.* **2018,** *30*, 1706287.

85. Wu, Y.; Jiang, Z.; Lu, X.; Liang, Y.; Wang, H., Domino Electroreduction of CO_2 to Methanol on a Molecular Catalyst. *Nature* **2019,** *575*, 639-642.

86. Yang, H.; Wu, Y.; Li, G.; Lin, Q.; Hu, Q.; Zhang, Q.; Liu, J.; He, C., Scalable Production of Efficient Single-Atom Copper Decorated Carbon Membranes for CO_2 Electroreduction to Methanol. *J. Am. Chem. Soc.* **2019,** *141*, 12717-12723.

87. Pan, F.; Deng, W.; Justiniano, C.; Li, Y., Identification of Champion Transition Metals Centers in Metal and Nitrogen-Codoped Carbon Catalysts for CO_2 Reduction. *Appl. Catal. B: Environ.* **2018,** *226*, 463-472.

88. Yang, F.; Song, P.; Liu, X.; Mei, B.; Xing, W.; Jiang, Z.; Gu, L.; Xu, W., Highly Efficient CO_2 Electroreduction on ZnN_4-based Single-Atom Catalyst. *Angew. Chem. Int. Ed.* **2018,** *57*, 12303-12307.

89. Chen, Z.; Mou, K.; Yao, S.; Liu, L., Zinc-Coordinated Nitrogen-Codoped Graphene as an Efficient Catalyst for Selective Electrochemical Reduction of CO_2 to CO. *ChemSusChem* **2018,** *11*, 2944-2952.

90. Zhang, E.; Wang, T.; Yu, K.; Liu, J.; Chen, W.; Li, A.; Rong, H.; Lin, R.; Ji, S.; Zheng, X.; Wang, Y.; Zheng, L.; Chen, C.; Wang, D.; Zhang, J.; Li, Y., Bismuth Single Atoms Resulting from Transformation of Metal–Organic Frameworks and Their Use as Electrocatalysts for CO_2 Reduction. *J. Am. Chem. Soc.* **2019,** *141*, 16569-16573.

91. Zhao, Y.; Liang, J.; Wang, C.; Ma, J.; Wallace, G. G., Tunable and Efficient Tin Modified Nitrogen-Doped Carbon Nanofibers for Electrochemical Reduction of Aqueous Carbon Dioxide. *Adv. Energy Mater.* **2018,** *8*, 1702524.

92. Zu, X.; Li, X.; Liu, W.; Sun, Y.; Xu, J.; Yao, T.; Yan, W.; Gao, S.; Wang, C.; Wei, S.; Xie, Y., Efficient and Robust Carbon Dioxide Electroreduction Enabled by Atomically Dispersed $Sn^{\delta+}$ Sites. *Adv. Mater.* **2019,** *31*, 1808135.

93. Zhao, K.; Nie, X.; Wang, H.; Chen, S.; Quan, X.; Yu, H.; Choi, W.; Zhang, G.; Kim, B.; Chen, J. G., Selective Electroreduction of CO_2 to Acetone by Single Copper Atoms Anchored on N-Doped Porous Carbon. *Nat. Commun.* **2020,** *11*, 2455.

94. Wanzhen, Z.; Feng, C.; Qi, Z.; Zhongjian, L.; Bin, Y.; Lecheng, L.; Qinghua, Z.; Feng, H.; Xilin, W.; Yang, H., A Universal Principle to Accurately Synthesize Atomically Dispersed Metal-N_4 Sites for CO_2 Electroreduction. *Nano-Micro Lett.* **2020,** *12*, 108.

95. Jeong, H.-Y.; Balamurugan, M.; Choutipalli, V. S. K.; Jo, J.; Baik, H.; Subramanian, V.; Kim, M.; Sim, U.; Nam, K. T., Tris(2-benzimidazolylmethyl)amine-Directed Synthesis of Single-Atom Nickel Catalysts for Electrochemical CO Production from CO_2. *Chem. Eur. J.* **2018,** *24*, 18444-18454.

96. Yang, H. B.; Hung, S.-F.; Liu, S.; Yuan, K.; Miao, S.; Zhang, L.; Huang, X.; Wang, H.-Y.; Cai, W.; Chen, R.; Gao, J.; Yang, X.; Chen, W.; Huang, Y.; Chen, H. M.; Li, C. M.; Zhang, T.; Liu, B., Atomically Dispersed Ni(I) as the Active Site for Electrochemical CO_2 Reduction. *Nat. Energy* **2018,** *3*, 140-147.

97. Wang, Y.; Chen, Z.; Han, P.; Du, Y.; Gu, Z.; Xu, X.; Zheng, G., Single-Atomic Cu with Multiple Oxygen Vacancies on Ceria for Electrocatalytic CO_2 Reduction to CH_4. *ACS Catal.* **2018,** *8*, 7113-7119.

98. Cheng, Y.; Zhao, S.; Li, H.; He, S.; Veder, J.-P.; Johannessen, B.; Xiao, J.; Lu, S.; Pan, J.; Chisholm, M. F.; Yang, S.-Z.; Liu, C.; Chen, J. G.; Jiang, S. P., Unsaturated Edge-Anchored Ni Single Atoms on Porous Microwave Exfoliated Graphene Oxide for Electrochemical CO_2. *Appl. Catal. B: Environ.* **2019,** *243*, 294-303.

99. Pan, Y.; Lin, R.; Chen, Y.; Liu, S.; Zhu, W.; Cao, X.; Chen, W.; Wu, K.; Cheong, W.-C.; Wang, Y.; Zheng, L.; Luo, J.; Lin, Y.; Liu, Y.; Liu, C.; Li, J.; Lu, Q.; Chen, X.; Wang, D.; Peng, Q.; Chen, C.; Li, Y., Design of Single-Atom Co–N_5 Catalytic Site: A Robust Electrocatalyst for CO_2 Reduction with Nearly 100% CO Selectivity and Remarkable Stability. *J. Am. Chem. Soc.* **2018,** *140*, 4218-4221.

100. Baruch, M. F.; Pander, J. E.; White, J. L.; Bocarsly, A. B., Mechanistic Insights into the Reduction of CO_2 on Tin Electrodes using in Situ ATR-IR Spectroscopy. *ACS Catal.* **2015,** *5*, 3148-3156.

101. Firet, N. J.; Smith, W. A., Probing the Reaction Mechanism of CO_2 Electroreduction over Ag Films via Operando Infrared Spectroscopy. *ACS Catal.* **2016,** *7*, 606-612.

102. Gunathunge, C. M.; Li, X.; Li, J.; Hicks, R. P.; Ovalle, V. J.; Waegele, M. M., Spectroscopic Observation of Reversible Surface Reconstruction of Copper Electrodes under CO_2 Reduction. *J. Phys. Chem. C* **2017,** *121*, 12337-12344.

103. Heyes, J.; Dunwell, M.; Xu, B., CO_2 Reduction on Cu at Low Overpotentials with Surface-Enhanced in Situ Spectroscopy. *J. Phys. Chem. C* **2016,** *120*, 17334-17341.

104. Pander, J. E.; Baruch, M. F.; Bocarsly, A. B., Probing the Mechanism of Aqueous CO_2 Reduction on Post-Transition-Metal Electrodes using ATR-IR Spectroelectrochemistry. *ACS Catal.* **2016,** *6*, 7824-7833.

105. Qin, X.; Zhu, S.; Xiao, F.; Zhang, L.; Shao, M., Active Sites on Heterogeneous Single-Iron-Atom Electrocatalysts in CO_2 Reduction Reaction. *ACS Energy Lett.* **2019,** *4*, 1778-1783.

106. Wang, Y.; Arandiyan, H.; Scott, J.; Aguey-Zinsou, K.-F.; Amal, R., Single Atom and Nanoclustered Pt Catalysts for Selective CO_2 Reduction. *ACS Appl. Energy Mater.* **2018,** *1*, 6781-6789.

107. Wuttig, A.; Liu, C.; Peng, Q.; Yaguchi, M.; Hendon, C. H.; Motobayashi, K.; Ye, S.; Osawa, M.; Surendranath, Y., Tracking a Common Surface-Bound Intermediate during CO_2-to-Fuels Catalysis. *ACS Cent. Sci.* **2016,** *2*, 522-8.

108. Zhu, S.; Jiang, B.; Cai, W. B.; Shao, M., Direct Observation on Reaction Intermediates and the Role of Bicarbonate Anions in CO_2 Electrochemical Reduction Reaction on Cu Surfaces. *J. Am. Chem. Soc.* **2017,** *139*, 15664-15667.

109. Jin, L.; Seifitokaldani, A., In Situ Spectroscopic Methods for Electrocatalytic CO_2 Reduction. *Catalysts* **2020,** *10*, 481.

110. Chen, J. G., Electrochemical CO_2 Reduction via Low-Valent Nickel Single-Atom Catalyst. *Joule* **2018,** *2*, 587-589.

111. Jeong, H.-Y.; Balamurugan, M.; Choutipalli, V. S. K.; Jeong, E.-s.; Subramanian, V.; Sim, U.; Nam, K. T., Achieving Highly Efficient CO_2 to CO Electroreduction Exceeding 300 mA cm^{-2} with Single-Atom Nickel Electrocatalysts. *J. Mater. Chem. A* **2019,** *7*, 10651-10661.

112. Ju, W.; Bagger, A.; Hao, G. P.; Varela, A. S.; Sinev, I.; Bon, V.; Roldan Cuenya, B.; Kaskel, S.; Rossmeisl, J.; Strasser, P., Understanding Activity and Selectivity of Metal-Nitrogen-Doped Carbon Catalysts for Electrochemical Reduction of CO_2. *Nat. Commun.* **2017,** *8*, 944.

113. Pan, F.; Zhang, H.; Liu, Z.; Cullen, D.; Liu, K.; More, K.; Wu, G.; Wang, G.; Li, Y., Atomic-Level Active Sites of Efficient Imidazolate Framework-Derived Nickel Catalysts for CO_2 Reduction. *J. Mater. Chem. A* **2019,** *7*, 26231-26237.

114. Pan, Y.; Lin, R.; Chen, Y.; Liu, S.; Zhu, W.; Cao, X.; Chen, W.; Wu, K.; Cheong, W. C.; Wang, Y.; Zheng, L.; Luo, J.; Lin, Y.; Liu, Y.; Liu, C.; Li, J.; Lu, Q.; Chen, X.; Wang, D.; Peng, Q.; Chen, C.; Li, Y., Design of Single-Atom Co-N_5 Catalytic Site: A Robust Electrocatalyst for CO_2 Reduction with Nearly 100% CO Selectivity and Remarkable Stability. *J. Am. Chem. Soc.* **2018,** *140*, 4218-4221.

115. Shao, X.; Yang, X.; Xu, J.; Liu, S.; Miao, S.; Liu, X.; Su, X.; Duan, H.; Huang, Y.; Zhang, T., Iridium Single-Atom Catalyst Performing a Quasi-Homogeneous Hydrogenation Transformation of CO_2 to Formate. *Chem* **2019,** *5*, 693-705.

116. Yuan, C.-Z.; Liang, K.; Xia, X.-M.; Yang, Z. K.; Jiang, Y.-F.; Zhao, T.; Lin, C.; Cheang, T.-Y.; Zhong, S.-L.; Xu, A.-W., Powerful CO_2 Electroreduction Performance with N–Carbon Doped with Single Ni Atoms. *Catal. Sci. Technol.* **2019,** *9*, 3669-3674.

117. Yuan, C.-Z.; Zhan, L.-Y.; Liu, S.-J.; Chen, F.; Lin, H.; Wu, X.-L.; Chen, J., Semi-Sacrificial Template Synthesis of Single-Atom Ni Sites Supported on Hollow Carbon Nanospheres for Efficient and Stable Electrochemical CO_2 Reduction. *Inorg. Chem. Front.* **2020,** *7*, 1719-1725.

118. Zhang, H.; Li, J.; Xi, S.; Du, Y.; Hai, X.; Wang, J.; Xu, H.; Wu, G.; Zhang, J.; Lu, J.; Wang, J., A Graphene-Supported Single-Atom FeN_5 Catalytic Site for Efficient Electrochemical CO_2 Reduction. *Angew. Chem. Int. Ed.* **2019,** *58*, 14871-14876.

119. Zhao, Z.; Lu, G., Cu-Based Single-Atom Catalysts Boost Electroreduction of CO_2 to CH_3OH: First-Principles Predictions. *J. Phys. Chem. C* **2019,** *123*, 4380-4387.

120. Weinberg, W. H., Eley−Rideal Surface Chemistry: Direct Reactivity of Gas Phase Atomic Hydrogen with Adsorbed Species. *Acc. Chem. Res.* **1996,** *29*, 479-487.

121. Seifitokaldani, A.; Gabardo, C. M.; Burdyny, T.; Dinh, C. T.; Edwards, J. P.; Kibria, M. G.; Bushuyev, O. S.; Kelley, S. O.; Sinton, D.; Sargent, E. H., Hydronium-Induced Switching between CO_2 Electroreduction Pathways. *J. Am. Chem. Soc.* **2018,** *140*, 3833-3837.

122. Nie, X.; Luo, W.; Janik, M. J.; Asthagiri, A., Reaction Mechanisms of CO_2 Electrochemical Reduction on Cu(111) Determined with Density Functional Theory. *J. Catal.* **2014,** *312*, 108-122.

123. Huynh, M. H. V.; Meyer, T. J., Proton-Coupled Electron Transfer. *Chem. Rev.* **2007,** *107*, 5004-5064.

124. Shi, C.; Hansen, H. A.; Lausche, A. C.; Nørskov, J. K., Trends in Electrochemical CO_2 Reduction Activity for Open and Close-Packed Metal Surfaces. *Phys. Chem. Chem. Phys.* **2014,** *16*, 4720-4727.

125. Hori, Y.; Wakebe, H.; Tsukamoto, T.; Koga, O., Electrocatalytic Process of CO Selectivity in Electrochemical Reduction of CO_2 at Metal Electrodes in Aqueous Media. *Electrochim. Acta* **1994,** *39*, 1833-1839.

126. Lin, R.; Guo, J.; Li, X.; Patel, P.; Seifitokaldani, A., Electrochemical Reactors for CO_2 Conversion. *Catalysts* **2020,** *10*, 473.

127. Bagger, A.; Ju, W.; Varela, A. S.; Strasser, P.; Rossmeisl, J., Single Site Porphyrine-Like Structures Advantages over Metals for Selective Electrochemical CO_2 Reduction. *Catal. Today* **2017,** *288*, 74-78.

128. Skúlason, E.; Tripkovic, V.; Björketun, M. E.; Gudmundsdóttir, S.; Karlberg, G.; Rossmeisl, J.; Bligaard, T.; Jónsson, H.; Nørskov, J. K., Modeling the Electrochemical Hydrogen Oxidation and Evolution Reactions on the Basis of Density Functional Theory Calculations. *J. Phys. Chem. C* **2010,** *114*, 18182-18197.

129. Cui, X.; An, W.; Liu, X.; Wang, H.; Men, Y.; Wang, J., C_2N-Graphene Supported Single-Atom Catalysts for CO_2 Electrochemical Reduction Reaction: Mechanistic Insight and Catalyst Screening. *Nanoscale* **2018,** *10*, 15262-15272.

130. Back, S.; Lim, J.; Kim, N. Y.; Kim, Y. H.; Jung, Y., Single-Atom Catalysts for CO_2 Electroreduction with Significant Activity and Selectivity Improvements. *Chem. Sci.* **2017,** *8*, 1090-1096.

131. Liu, X.; Xiao, J.; Peng, H.; Hong, X.; Chan, K.; Norskov, J. K., Understanding Trends in Electrochemical Carbon Dioxide Reduction Rates. *Nat. Commun.* **2017,** *8*, 15438.

132. Peterson, A. A.; Nørskov, J. K., Activity Descriptors for CO_2 Electroreduction to Methane on Transition-Metal Catalysts. *J. Phys. Chem. Lett.* **2012,** *3*, 251-258.

133. Back, S.; Jung, Y., TiC- and TiN-Supported Single-Atom Catalysts for Dramatic Improvements in CO_2 Electrochemical Reduction to CH_4. *ACS Energy Lett.* **2017,** *2*, 969-975.

134. Tran, K.; Ulissi, Z. W., Active Learning across Intermetallics to Guide Discovery of Electrocatalysts for CO_2 Reduction and H_2 Evolution. *Nat. Catal.* **2018,** *1*, 696-703.

135. Wang, Z.; Zhao, J.; Cai, Q., CO_2 Electroreduction Performance of a Single Transition Metal Atom Supported on Porphyrin-Like Graphene: A Computational Study. *Phys. Chem. Chem. Phys.* **2017,** *19*, 23113-23121.

136. Choi, Y. W.; Mistry, H.; Roldan Cuenya, B., New Insights into Working Nanostructured Electrocatalysts through Operando Spectroscopy and Microscopy. *Curr. Opin. Electrochem.* **2017,** *1*, 95-103.

137. Li, X.; Wang, S.; Li, L.; Sun, Y.; Xie, Y., Progress and Perspective for In Situ Studies of CO_2 Reduction. *J. Am. Chem. Soc.* **2020,** *142*, 9567-9581.

138. Handoko, A. D.; Wei, F.; Jenndy; Yeo, B. S.; Seh, Z. W., Understanding Heterogeneous Electrocatalytic Carbon Dioxide Reduction through Operando Techniques. *Nat. Catal.* **2018,** *1*, 922-934.

139. Adarsh, K. S.; Chandrasekaran, N.; Chakrapani, V., In-situ Spectroscopic Techniques as Critical Evaluation Tools for Electrochemical Carbon Dioxide Reduction: A Mini Review. *Front. Chem.* **2020,** *8*.

140. Zhong, L.; Chen, D.; Zafeiratos, S., A Mini Review of In Situ Near-Ambient Pressure XPS Studies on Non-Noble, Late Transition Metal Catalysts. *Catal. Sci. Technol.* **2019,** *9*, 3851-3867.

141. Yang, H.; Lin, Q.; Zhang, C.; Yu, X.; Cheng, Z.; Li, G.; Hu, Q.; Ren, X.; Zhang, Q.; Liu, J.; He, C., Carbon Dioxide Electroreduction on Single-Atom Nickel Decorated Carbon Membranes with Industry Compatible Current Densities. *Nat. Commun.* **2020,** *11*, 593.

142. Möller, T.; Ju, W.; Bagger, A.; Wang, X.; Luo, F.; Ngo Thanh, T.; Varela, A. S.; Rossmeisl, J.; Strasser, P., Efficient CO_2 to CO Electrolysis on Solid Ni–N–C Catalysts at Industrial Current Densities. *Energy Environ. Sci.* **2019,** *12*, 640-647.

143. Suen, N.-T.; Hung, S.-F.; Quan, Q.; Zhang, N.; Xu, Y.-J.; Chen, H. M., Electrocatalysis for the Oxygen Evolution Reaction: Recent Development and Future Perspectives. *Chem. Soc. Rev.* **2017,** *46*, 337-365.

144. Lu, X.; Zhao, C., Electrodeposition of Hierarchically Structured Three-Dimensional Nickel–Iron Electrodes for Efficient Oxygen Evolution at High Current Densities. *Nat. Commun.* **2015,** *6*, 6616.

145. Chen, Y.; Vise, A.; Klein, W. E.; Cetinbas, F. C.; Myers, D. J.; Smith, W. A.; Deutsch, T. G.; Neyerlin, K. C., A Robust, Scalable Platform for the Electrochemical Conversion of CO_2 to Formate: Identifying Pathways to Higher Energy Efficiencies. *ACS Energy Lett.* **2020,** *5*, 1825-1833.

146. Gabardo, C. M.; O'Brien, C. P.; Edwards, J. P.; McCallum, C.; Xu, Y.; Dinh, C.-T.; Li, J.; Sargent, E. H.; Sinton, D., Continuous Carbon Dioxide Electroreduction to Concentrated Multi-carbon Products Using a Membrane Electrode Assembly. *Joule* **2019,** *3*, 2777-2791.

Table of Contents graphic: